



Mie Scattering for Photonic Devices

Review Article**Author(s):**

Dorodnyy, Alexander; [Smajic, Jasmin](#) ; [Leuthold, Juerg](#) 

Publication date:

2023-09

Permanent link:

<https://doi.org/10.3929/ethz-b-000623817>

Rights / license:

[Creative Commons Attribution-NonCommercial 4.0 International](#)

Originally published in:

Laser & Photonics Reviews 17(9), <https://doi.org/10.1002/lpor.202300055>

Mie Scattering for Photonic Devices

Alexander Dorodnyy,* Jasmin Smajic, and Juerg Leuthold

Mie scattering is increasingly exploited to manipulate electromagnetic fields to achieve strong resonant enhancement, to obtain perfect absorption of radiation, and to generate polarization or wavelength selectivity and/or sensitivity. In fact, a multitude of photonic applications are arising that benefit from Mie scattering and have already led to the formation of novel image and hologram schemes or to the design of efficient and compact photodetectors and light sources. Here, the Mie scattering theory for spherical scatterers is reviewed, the basics of the field-decomposition onto the Mie modes are shown, and dielectric and metallic particles are compared. Recent applications for light spectrum control, detection, non-linear effects enhancement, and emission are reviewed. How a periodic arrangement of Mie-scatterers can be utilized to create a strong (in the order of 10 to 100) absorption enhancement in otherwise weakly absorbing layers is also demonstrated. The enhancement dependence on the diameter-to-wavelength ratio of the scatterer is analyzed, and how the influence of different Mie-modes can be distinguished in the periodic array by looking at the field components normal to the scatterer surface is discussed.

1. Introduction

Scattering of light by nanostructured materials is a vast topic that covers applications from light filtering and guiding^[1–7] to various detection,^[8–14] emission, and high-harmonic generation schemes.^[15–21] At the core of these applications is the ability of tiny particles to support oscillation modes of electric and magnetic nature that can redirect, enhance or absorb the electromagnetic field. Despite their small size such particles may be efficient light scatterers as they can attract light from the cross-section multiple times exceeding their own geometrical size. The modes that are excited within such particles are commonly referred to as Mie-resonances. The theory first suggested by Gustav Mie in 1908^[22] describes the decomposition of the scattered field into

a set of harmonics starting with the dipole then quadrupole, octupole, and higher-order multipoles of either electric or magnetic nature.

The advancements in processing technologies have led to a rapid increase in applications that rely on nanostructured materials. This includes applications that take advantage of nano-scatterers such as Mie-resonators. For instance, the widely used CMOS technology with its reproducible processes and an ever-better resolution has been made accessible to photonics with processes originally designed only for electronics. Since the effects associated with Mie-scattering can be realized with a large variety of scatterer materials, Mie-scatterers are naturally suitable to be incorporated in a CMOS process that is strict in terms of available materials.^[23–28] Furthermore, fabrication technologies such as nano-imprint or Talbot lithography^[29–33] now enable large-

scale fabrication of nanostructured features that so far have only been available to expensive e-beam lithography. Nano-imprint processes are naturally favoring structures with a single patterned layer. As such, it is important to note that in case of Mie-scattering a multitude of effects such as strong field enhancement, high-Q resonances, perfect light absorption, etc. can be achieved within just a single nanostructure layer. More so, even within a single layer, due to the localized nature of Mie modes (i.e., a single particle exhibits the characteristic scattering patterns), a random distribution of Mie scatterers is often sufficient. This allows for instance the deposition of dispersed colloiddally synthesized particles on virtually any surface. For example, such dispersed Mie-resonators were demonstrated to work for color-generation via control of the size of dispersed particles.^[1,34,35]

Mie-resonances are commonly associated with a wide variety of optical effects. Effects that have their origin in a wealth of rather intricate superpositions of scattering modes excited by the external field. Of practical relevance is the formation of localized high-Q resonances. They typically form if scattered fields are trapped to the particle (weakly coupled to the external radiation) and if internal losses are low. The Q-factor of such resonances can exceed 10^6 in theory.^[36] The resonant structures based on Mie modes can be used for a multitude of purposes from light filtering^[1,37–42] and sensing^[43] to the creation of field-enhancement,^[44,45] which is, e.g., useful for nonlinear applications such as the high-order harmonic generation^[46–48] or light emission and lasing.^[15,49–54]

Another effect closely connected to the formation of highest Q-factor modes is the existence of nonradiative states.^[2,55] Modes

A. Dorodnyy, J. Smajic, J. Leuthold
ETH Zurich
Institute of Electromagnetic Fields (IEF)
Gloriastrasse 35, Zurich 8092, Switzerland
E-mail: alexander.dorodnyy@ief.ee.ethz.ch

 The ORCID identification number(s) for the author(s) of this article can be found under <https://doi.org/10.1002/lpor.202300055>

© 2023 The Authors. Laser & Photonics Reviews published by Wiley-VCH GmbH. This is an open access article under the terms of the Creative Commons Attribution-NonCommercial License, which permits use, distribution and reproduction in any medium, provided the original work is properly cited and is not used for commercial purposes.

DOI: 10.1002/lpor.202300055

that are related to this phenomenon are commonly divided into two types: 1) anapoles (such as ones created by superposition of standard multipole and toroidal modes)^[36,56–61] and 2) bounded states in continuum (BiC).^[55,62] The toroidal modes are formed by electric currents inside a nanoparticle that appear as if the current would be floating on a surface of a toroid.^[55,59,60,63,64] The radiation from toroidal modes is identical to the electric multipole emissions described above. A superposition of a toroidal mode with a multipole mode of corresponding order may give rise to a current pattern inside the particle that does not produce far-field radiation. It is also worth mentioning that toroidal modes are commonly considered in literature from two different angles: In some works the behavior of scattering amplitudes in the far field has been found to possess frequencies where scattering amplitudes vanish while the amplitudes of the modes inside the scatterer are high.^[64,65] In other works the decomposition into harmonics is done for the charge and current distribution in the scatterer and an extra set of toroidal modes is found in addition to the multipoles described above that exhibit qualitatively the same behavior as in the previous approach.^[66] Theoretically, two types of toroidal modes can exist. One is composed of a circular arrangement of magnetic dipoles and another of electric dipoles. However, the latter would require existence of magnetic sources.^[63,66] Regardless of the interpretation, the anapole modes can't directly couple to the external radiation, but under certain conditions, they may give rise to weakly outcoupled modes with high Q-factors. Worth to note that the anapole can't couple to the external radiation in a steady state. However, under transient conditions such coupling is possible.^[67] In Section S5 of the Supporting Information, we discuss that phenomenon in more detail.

Yet, another interesting phenomenon is critical coupling. It is obtained when all the energy flowing into the resonator, will dissipate non-radiatively within the resonator. Commonly, that implies the existence of at least two modes that destructively interfere to prevent radiation of the energy to the outside. For obtaining critical coupling the Q-factor needs to be adjusted to the non-radiative decay rate.^[68–70] It is worth noting that although there is an absorption limit associated with a single scatterer of arbitrary shape,^[71–73] in the presence of an array of scatterers due to the possible reabsorption of light scattered by one particle by its neighbors' nearly-complete absorption of the incoming wave is possible.^[68,74]

Mie modes can also sum up to radiate into a particular direction.^[3,49] A special situation of full canceling of the forward or backward radiation is known as the Kerker effect. In practice, this allows removing reflection (back-scattering), filtering out some of the frequencies in the forward-direction (by removing forward scattering), or diverting the light, for example, by 90 degrees to propagate and be absorbed in a layer perpendicular to the initial light propagation direction. An interesting variation of redirection is the use of Mie-resonances to create waveguiding structures that allow for ultra-compact yet efficient waveguides that are also robust against processing inaccuracies. Another effect associated with the interaction of Mie modes of different orders are the Fano resonances.^[75–78] These resonances appear due to an interaction of resonance with broader modes or a continuum of states. In the case of Mie-scatterers, they commonly appear due to an interaction of modes of a different order – such as the interaction of a dipole with a quadrupole mode. Fano res-

onances exhibit high sensitivity to the surroundings of the scatterer and can be used for sensitive sensing/imaging. They have also been employed in lasers and slow-light devices.^[79–82]

In this paper, we first present an overview of Mie-scattering. We give a brief summary of the scattering of a plane electromagnetic wave impinging on a sphere. A derivation of the Mie-solution in terms of a multipole expansion in spherical coordinates is given in Supplementary Information. The electrical and magnetic Mie scattering modes are given and lower-order modes with the electric and magnetic fields are plotted. The near- and far-fields of the modes and their physical origin is discussed. The difference between mode excitations in dielectric and metallic particles is then outlined. We continue with an overview of some representative ideas and applications related to Mie-scattering. Finally, we conclude the paper with a discussion on Mie scattering of an incident field into a plane, which is relevant for sensing and detection.

2. Mie Scattering

Upon interacting with a nanoparticle, electromagnetic radiation can produce dipole, quadrupole, and higher-order resonances. More precisely, the incident electrical fields induce charge oscillations that polarize the scatterer. This polarization oscillates with the incident electric field producing electromagnetic radiation. In a similar fashion, the incident magnetic field induces circular currents within the scatterer that – when oscillating with the incident magnetic field – also produces electromagnetic radiation. These charge/current oscillations of electric and magnetic nature are known as Mie-modes (or multipoles).

Here we will consider the case of a spherical scatterer under a plane-wave excitation shown in **Figure 1**. For the case of a spherical scatterer, we can find analytical solutions in terms of spherical harmonics which will be the eigenmodes of that scattering problem. The superposition of all of these modes results in characteristic near and far fields (see **Figures 2 and 3**).

Naturally, the shape of the scatterer matters. The Mie-modes discussed further below are eigenmodes in case of a perfectly round sphere. However, for other shapes such as nanocubes, nanocylinders, and many other shapes, it is still reasonable to describe the optical response in terms of Mie-modes since the qualitative characteristics of the scattering picture stay the same. For example, on a cubic particle, one still will observe the consecutive appearance of electric and magnetic dipoles, quadrupoles, and higher-order modes with identical far-field distributions as for the case of the sphere.

In the following, we will consider a spherical particle of radius R (diameter $D = 2R$) of permittivity ϵ_b and permeability μ_b (index “b” here denotes the bounded domain within the scatterer) in a vacuum (formally assigned with permittivity ϵ_s and permeability μ_s for the sake of generosity where “s” stands for the scattered-field domain around the particle). A single-frequency plane wave is impinging onto the particle. The incident electromagnetic wave i with the wave polarized as shown in the figure is given by the fields \vec{E}_i and \vec{H}_i , see **Figure 1**. The field inside the sphere is denoted by index “b” and the scattered field is denoted by an index “s”. For symmetry reasons, we use spherical coordinates (r, θ, φ) as it is shown in the figure.

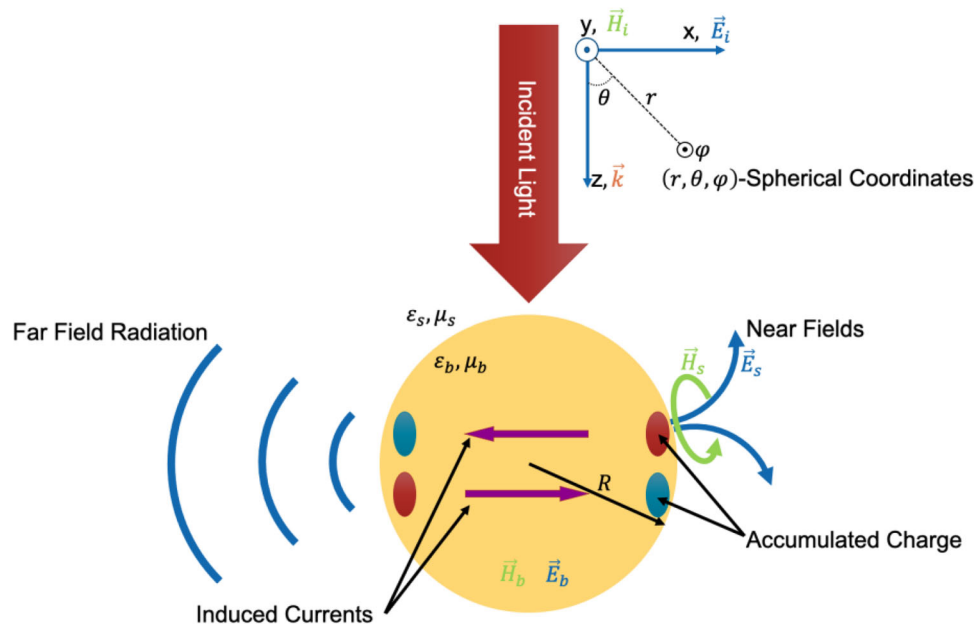


Figure 1. Schematic illustration of the considered scattering problem. The incident plane wave is linearly polarized with E-fields along the x-axis. The coordinate system is aligned with the incident fields \vec{E}_i and \vec{H}_i . Inside the bound region, (index “b”) of the spherical scatterer with radius R , linear and circular currents are induced. In the figure, we show, e.g., by a pink pointer a linear current due to an electrical field excitation. In response accumulated charges accumulate on the surface. This charge is oscillating with the incident electric field producing electromagnetic radiation and creating characteristic (for each Mie-mode) near-field patterns (see Figure 2). The scattered fields outside of the particle are denoted by index “s”. The spherical coordinates needed to find the analytical solution to the scattering problem are defined in the cartesian coordinate system as shown on top.

Let’s first consider how the electromagnetic field that passes through the particle excites different electric and magnetic Mie-modes. Due to the symmetry of the problem, only a selected subset of the Mie-modes will be excited based on the polarization and propagation direction of the incident wave. Specifically, only Mie-modes that have $\sin(\varphi)$ or $\cos(\varphi)$ dependence on the spherical coordinate φ will be excited, whereas the excitation of the modes with $\sin(m\varphi)$ or $\cos(m\varphi)$ with $m \neq 1$ will be forbidden by the symmetry of the plane wave excitation. Modes with other m -values can, e.g., be excited by a combination of several plain-waves.

The incident electric field excites charge oscillations within the scatterer. As a result, charge-nodes are being formed along the passage of the light through and around the scatterer as shown in Figure 2, see the pink pointers in subset (a1– c1). The shorter the wavelength or the larger the particle – the more nodes can be created inside the particle and the higher-order Mie-modes can be excited. For a dipole a single node with two charges on opposite sides is created, see Figure 2(a1); for the quadrupole two nodes that are oriented oppositely in terms of the charge and current emerge, see Figure 2(b1), and so forth. For the incident magnetic field, a similar principle applies with the exception that the incident magnetic field is inducing current loops within the scatterer around the incident magnetic flux. These current loops do not produce a net change in the charge density, so no normal electric fields are observed on the surface of the scatterer, see Figure 2 subset (a2–c2). Similar to the currents in the case of electric modes the induced currents in a magnetic mode alternate the direction (of the current loop) from one node to the next.

To find the decomposition of the scattered fields on the modes shown in Figure 2 one needs to solve the problem for the particle given in Figure 1. This can be solved analytically by using the spherical coordinate system (see Supplementary Information for the full-solution, see also^[83]). The solutions of both the bound and scattered electromagnetic fields have the form

$$\vec{E} = \sum_{l,m} \left(p_{m,l} \vec{T}_{m,l}^a + q_{m,l} \vec{S}_{m,l}^b \right) \quad (1.1)$$

$$\vec{H} = -i \sqrt{\frac{\epsilon}{\mu}} \sum_{l,m} \left(p_{m,l} \vec{S}_{m,l}^a + q_{m,l} \vec{T}_{m,l}^b \right), \quad (1.2)$$

where functions \vec{T} and \vec{S} define the basic vector fields of the modes. Specifically, \vec{S} is the field with its source located in the scatterer. \vec{S}^b is the electric field generated by the electric multipole charges and \vec{S}^a is the magnetic field generated by the loop currents of magnetic multipoles. One can see from Figure 2 that the \vec{S} fields are fields with a normal component that flows in and out of the scatterer. Whereas \vec{T} represents the contributions from the induced fields. \vec{T}^b are magnetic fields of the electric modes. \vec{T}^a are the electric fields of the magnetic modes. In Figure 2 these fields are encircling the “source” fields in the direction corresponding to the electric or magnetic induction. These fields are oriented along the surface of the scatterer. The vector functions \vec{T} and \vec{S} are found to be (see Supplementary Information)

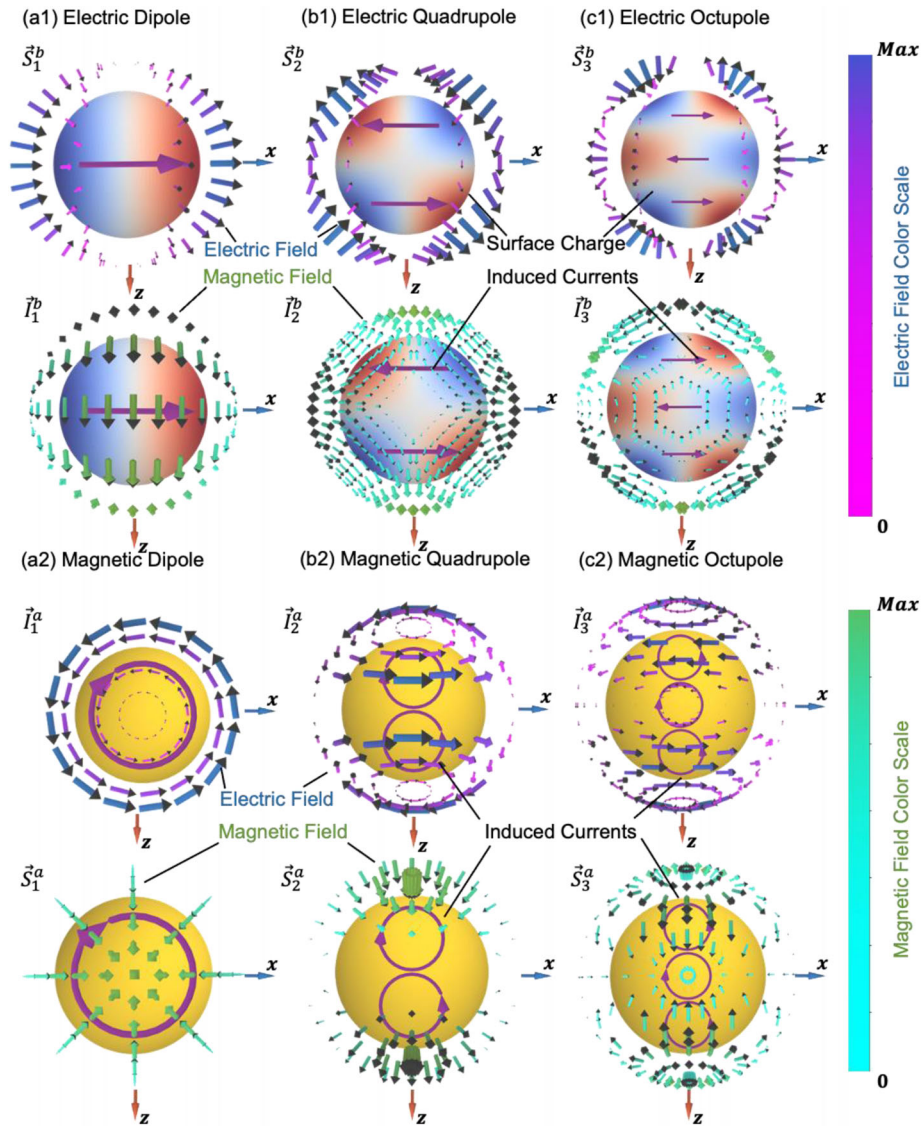


Figure 2. Schematic illustration of Mie-scattering situation (near-field). A linearly polarized (E-field shown by blue arrows, magnetic by green) plane wave excitation is scattered by a spherical nanoparticle. The field of the Mie-modes near the surface of the scatterer are shown for electric and magnetic dipole/quadrupole/octupole modes. a1–c1) Electric modes. a2–c2) Magnetic modes. The induced linear and circular currents as induced by the electric and magnetic fields are shown by purple arrows. In case of electric modes the current flows in a linear fashion leading to formation of the surface charges whereas in case of magnetic modes the looped currents do not cause any electrical polarization. The charge densities on the surface of the sphere as created by the electric fields are shown by the blue and red colors. The maximal magnitude values of the displayed fields (E/H) are 4.7, 1.2, 3.0, 3.3, 2.5, 2.9 for electric (dipole, quadrupole, octupole) and magnetic modes in the same order respectively (values are taken in SGS system). 3D models shown in the figure can be found at: https://ief.ee.ethz.ch/education/Educational_Materials.html.

$$\begin{aligned}
 & \vec{I}_{l,m}^a = \frac{m}{\sin(\theta)} z_l(kr) P_l^m(\cos(\theta)) \left\{ \begin{array}{l} \cos(m\varphi) \vec{e}_\theta - \sin(m\varphi) \vec{e}_\varphi \\ \sin(m\varphi) \vec{e}_\theta + \cos(m\varphi) \vec{e}_\varphi \end{array} \right\} \\
 & \vec{S}_{l,m}^a = \frac{l(l+1)}{kr} z_l(kr) P_l^m(\cos(\theta)) \left\{ \begin{array}{l} \sin(m\varphi) \vec{e}_r + \frac{1}{kr} \frac{d}{dr} (rz_l(kr)) \frac{d}{d\theta} P_l^m(\cos(\theta)) \left\{ \begin{array}{l} \sin(m\varphi) \vec{e}_\theta \\ \cos(m\varphi) \vec{e}_\varphi \end{array} \right\} \\ + \frac{m}{kr \sin(\theta)} \frac{d}{dr} (rz_l(kr)) P_l^m(\cos(\theta)) \left\{ \begin{array}{l} \cos(m\varphi) \vec{e}_\theta \\ -\sin(m\varphi) \vec{e}_\varphi \end{array} \right\} \end{array} \right. \quad (1.3)
 \end{aligned}$$

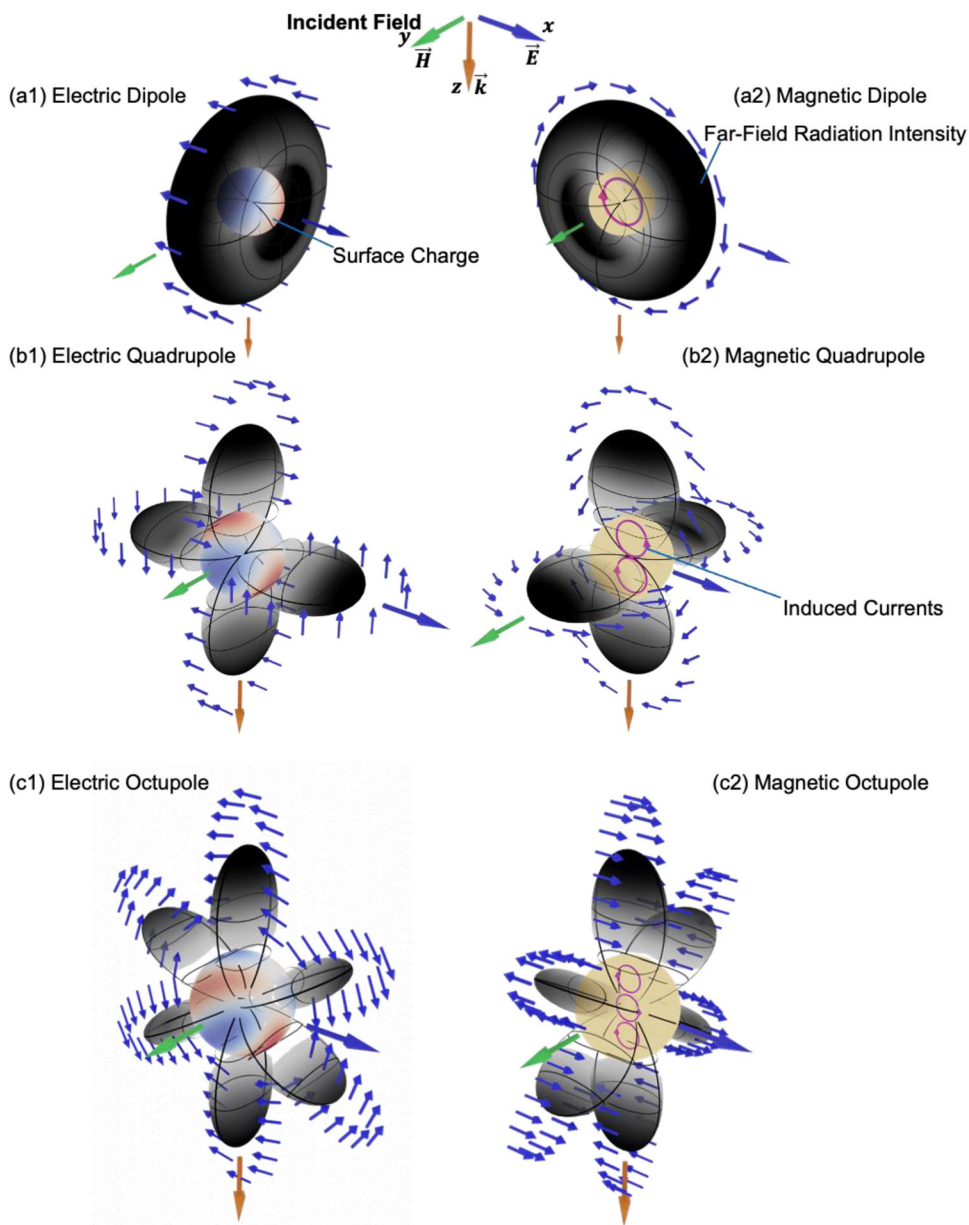


Figure 3. a1-c1) Far field radiation of electric dipole/quadrupole/octupole modes. a2-c2) The higher-order modes create multiple radiation beams each having its origin in a charge oscillation in the scatterer. In case of electric modes, the far-field polarization is aligned with the polarization pattern of the scatterer whereas in the case of magnetic modes the electric polarization is defined by the induced current loops.

Here, k is the magnitude of the wavevector at the incident frequency in the corresponding material, (r, θ, φ) are the spherical coordinates, (l, m) are spherical harmonic numbers, and (a, b) denote the two types of φ -dependence that the problem symmetry allows, $\sin(m\varphi)$ and $\cos(m\varphi)$, respectively. In our case, as mentioned above, $m = 1$ for an incident plane field. $m \neq 1$ would apply to a situation with an arbitrarily polarized incident field. Yet, since such fields are superpositions of linear plane waves alike, it is sufficient to discuss the case $m = 1$. One can also notice that upon switching from electric to magnetic modes the roles of \vec{I} and \vec{S} are switching places (plus they rotate by 90 degrees around

the z -axis due to the fixed light polarization). This symmetry relation was to be expected due to the symmetry of the Maxwell equations and the absence of consideration of the boundary conditions so far.

The near-field evolves into far-fields as displayed in Figure 3. One may notice that in the case of electric modes, the charge-pairs on the surface of the scatterer induce a burst of radiation similar to a dipole. A similar pattern is observed for the magnetic Mie-modes where current loops induce electromagnetic field radiation. The analytical expression for the far-field radiation can be found in Supplementary Information.

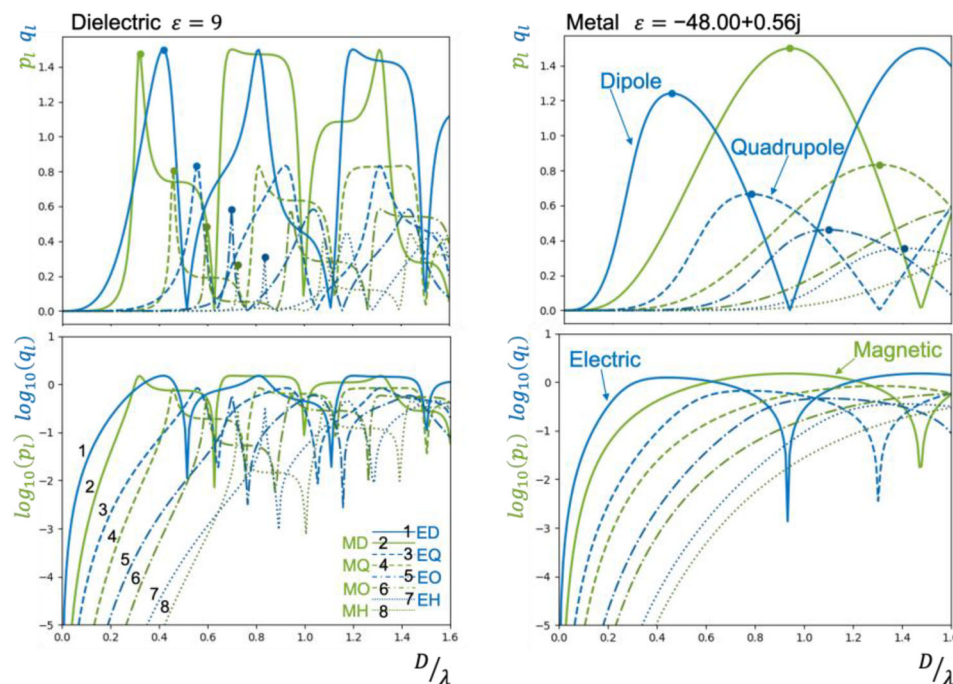


Figure 4. Illustration of mode amplitudes for dielectric and metal scatterers in linear and logarithmic scales. Two differences between dielectric and metallic scatterers can be seen: 1) Dielectric scatterers provide a vivid pattern of amplitude oscillations that are due to the interference of scattered and bound Mie modes. A recurring pattern of resonances can be seen in the dielectric sphere. 2) Metallic modes feature fewer resonances as fields are forced out of the scatterer, leading to less options for constructive and destructive interferences. The permittivity values of the materials are shown in the figure. The metal permittivity corresponds to silver at $\approx 1 \mu\text{m}$. From the derivation of the Mie theory given in Supporting Information, one can also see that in the absence of the material dispersion, the mode amplitudes only depend on the diameter-to-wavelength ratios of the scatterer. In the legend letters “M” and “E” stand for Magnetic and Electric, letters “D”, “Q”, “O” and “H” are for Dipole, Quadrupole, Octupole, Hexadecapole correspondingly.

Up to now, we only looked at the solution decomposition in terms of the spherical harmonics, but we did not discuss the amplitudes of these harmonics defined by the boundary conditions. The latter is what eventually differentiates electric and magnetic modes. It is also the reason for differences between scattering patterns of metal and dielectric particles. Metallic and dielectric nano-scatterers have quite different modal amplitudes, see **Figure 4**.

For both dielectric and metallic spheres, the modes have resonant behavior in dependence on the diameter-to-wavelength of the scatterer. One can notice from **Figure 4** that for the case of dielectric scatterers, a more complex pattern with more frequent oscillations can be seen when compared to the case of metal scatterer. The latter happens because in case of metals the electromagnetic field is pushed out of the scatterer and the modes can couple to the external field only when the incident wave outside the scatterer coincides with the charge-periodicity of the mode on the surface. For the dielectrics, on the contrary, coupling is possible both via the charge on the surface and via the field that penetrates inside the scatterer. The latter causes an extra set of resonant peaks in the mode amplitudes. Furthermore, for the same reason of the electric field being pushed out of the metal, the magnetic modes of a metal sphere are pushed away from the subwavelength regime and only peak at the scale of nanoparticles comparable with wavelength. That happens because a current loop can't be created within the metal and has to occur on its surface leading to the excitation peak of the first (dipole) mode appearing

only when the loop can be big enough to encircle the whole particle. Additionally, metallic particles will exhibit losses associated with their finite conductivity which is discussed in more detail further below in **Figure 6**.

Figure 5 shows the dependency of the full field intensity (summed up over all significantly excited modes) for metal and dielectric scatterers in dependence on the diameter-to-wavelength ratio. In both cases, Rayleigh scattering is observed for the deep subwavelength particle sizes that represent the electric-dipole mode. With increase in size, due to the simultaneous presence of electric and magnetic modes in the dielectric, special phenomena such as forward-only scattering can be observed for the dielectric scatterer, see the second intensity plot in **Figure 5a**. This is also known as the Kerker effect. The phenomena can be best understood from **Figure 4**. For $D = 0.29\lambda$ the amplitudes of electric and magnetic dipoles are the same in magnitude, however, due to the opposite symmetry of the produced fields against the xy -planes, see **Figure 3(a1),(b2)** the modes add constructively forward and destructively backward resulting in forward-only scattering. Further on as more modes are excited in the dielectric complex scattering patterns emerge that eventually translate into geometrical optics. Two notable cases can be seen for the values of $D = 0.63\lambda$ and $D = 0.69\lambda$. In the first case the scattering is strongly lateral with nearly-zero scattering backwards. This can be useful for enhancing light absorption in laterally oriented layers while simultaneously removing the reflected component of the light. The second case corresponds to

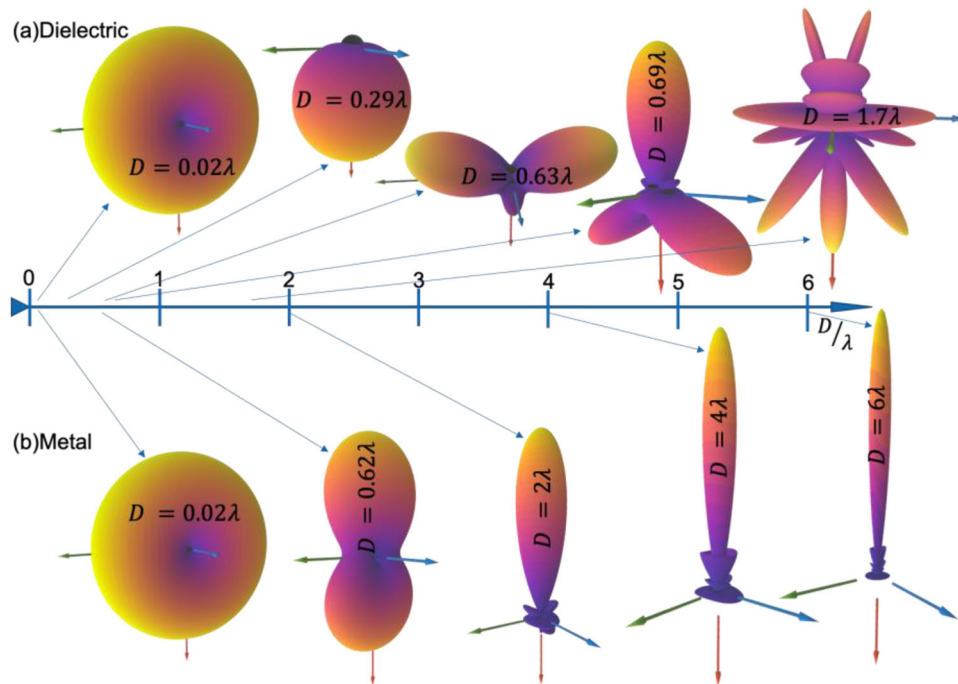


Figure 5. Illustration of full scattered field intensity (summed up over all significant modes) for b) metal and a) dielectric particles with several diameter-to-wavelength ratios. In both cases, Rayleigh scattering with its toroid shape is observed for small particles. As particle size increases the dielectric radiation pattern undergoes multiple characteristic patterns. One can recognize a Kerker scattering at $D = 0.29$, a pronounced lateral scattering, and a blocked forward scattering. The metallic particle evolves increasingly toward a full reflector with a diameter size.

the strong lateral and back scattering with no light being scattered forward. This case can be used for filtering the passing radiation to create, for example, inverted colors. For the case of the metal scatterer, one can observe the transition to geometrical optics in **Figure 6** as the scatterer becomes a simple reflector with the increase of its diameter-to-wavelength ratio.

Another notable feature of metallic scatterers that is not present in the case of dielectrics is the plasmon resonance. **Figure 6** shows the behavior of the total scattering/absorption cross-sections (normalized on the geometrical cross-section of the scatterer) for the case of a) dielectric, b) a metal far away from the plasmon resonance, and c) a metal close to the plasmon resonance. One can see that for all cases the scattering cross-section G_s drops fast as the particle size becomes much smaller than the wavelength. For the case of the metal (away from plasmon resonance) there is also the absorption cross-section G_a which is however much smaller than 1 due to the high reflection of the metal in this frequency range. For the case of the metal near the plasmon resonance, however, the pattern is different – due to the plasmon excitation a considerable absorption cross-section is observed which is also not dropping with the size decrease as sharply as the scattering cross-section. The latter allows metallic particles of just a few nanometers in size to exhibit strong resonances at optical frequencies. It is worth noting however that classical consideration used here stops holding for the case of few nanometers and smaller particles where more detailed models of carrier behavior in the scatterer need to be considered such as models taking into account non-local effects.^[84–86] Finally, one can observe how the backward-forward scattering ratio behaves for the

metals and dielectrics (see bottom of **Figure 6**). In all cases the forward-backward scattering ratio R_{bf} starts with 0.5 which corresponds to the symmetric Rayleigh scattering. For the dielectrics then it starts oscillating where periodically the backward scattering is suppressed by essentially the anti-reflection coating effect when the wave reflected back in the particle cancels the one reflected by its front surface. For the metal cases, the backward reflection eventually dominates the forward scattering with the more absorptive metal losing its forward scattering faster due to the plasmon absorption (to be scattered forward light need to couple to the plasmon propagating around the surface first).

To sum up, the difference between metallic and dielectric Mie-modes are mainly: a) Losses due to the movement of free carriers in a metal; b) Low-penetration depth of the field into the metal particles. The first factor limits the quality-factor available to metallic structures but allows to create conductive nano-resonators that can have a double-fold purpose of serving as electric contact layers and microwave circuits.^[87–89] The second factor limits the scale of current loops that can exist on the metal nanoparticle pushing the magnetic modes outside of the subwavelengths particle scale, leaving smallest metallic Mie-scatterers with dominant electric modes.

It is worth noting that for most practical devices, a single Mie-scatterer is not sufficient to achieve the desired effect. So an arrangement such as a periodic 2D or 1D array is often required. For such arrays due to the interaction between neighboring scatterers, it is sometimes possible to describe the far-field analytically.^[90] Extra modes are then appearing due to the superpositions of radiation from the scatterers (grating-effects).

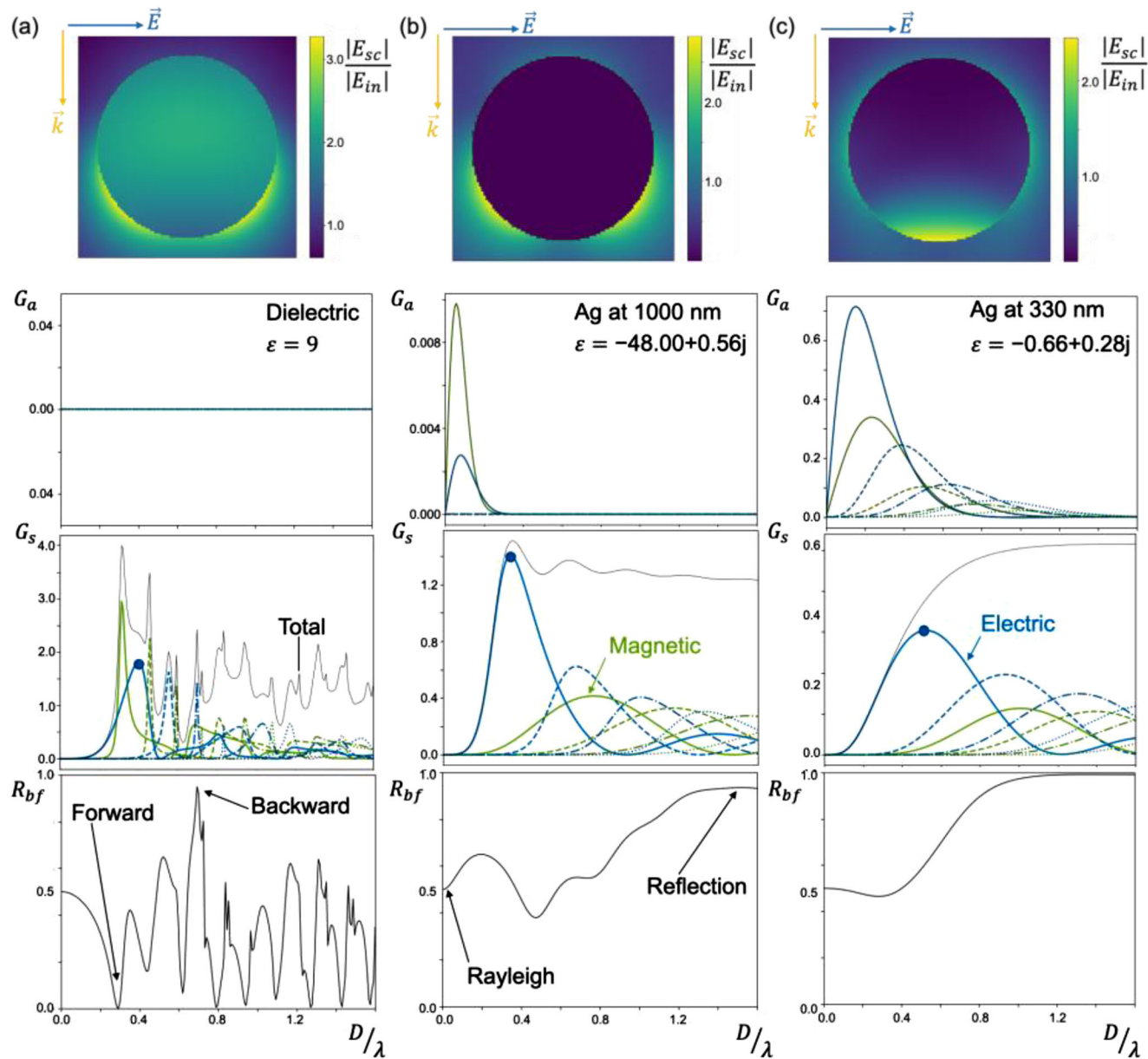


Figure 6. Absorption/scattering cross-sections and backward-forward scattering ratio for the cases of (a) dielectric, (b) silver at 1000 nm (where metal is highly-reflective) and (c) silver at 330 nm (closer to plasmonic resonance at around 140 nm). Here we use the following notation G_a and G_s are absorption and scattering cross-sections normalized by the power within the scatterer geometrical cross-section; R_{bf} is the ratio of the backward scattering intensity “BW” against the sum of the forward “FW” and backward scattering, defined by the equation $R_{bf} = BW / (FW + BW)$. One can observe the strong dominance of the scattering G_s against absorption G_a for the case of silver away from the plasmon resonance. Whereas for the case close to the resonance the absorption cross-section stays significant even for the deep subwavelength sizes of the scatterer. The latter illustrates the plasmon effect that can be observed on particles of only a few nanometers in size. Diameter-to-wavelength ratio values for each of the field plots are chosen for the first maximum of electrical dipole mode as it is marked by blue dots on the scattering plots.

However, while new constructive and destructive patterns appear, they still stem from the single particle behavior.^[91,92] For example, modes of opposite symmetry required for perfect absorption in a flat layer are originating from the modes on a single particle.^[68] Similarly, toroidal modes reported on cuboid arrays are originating from the geometry of a single scatterer.^[58]

In the following sections, we will consider some instructive recent applications that show how Mie-scattering can be used for

spectrum management, photodetection and to build novel light sources.

3. Mie-Scattering for Device Applications

In the following sections, we will overview some of the notable works on application of Mie-scattering to spectrum management, absorption/detection, and tailored emission of radiation.

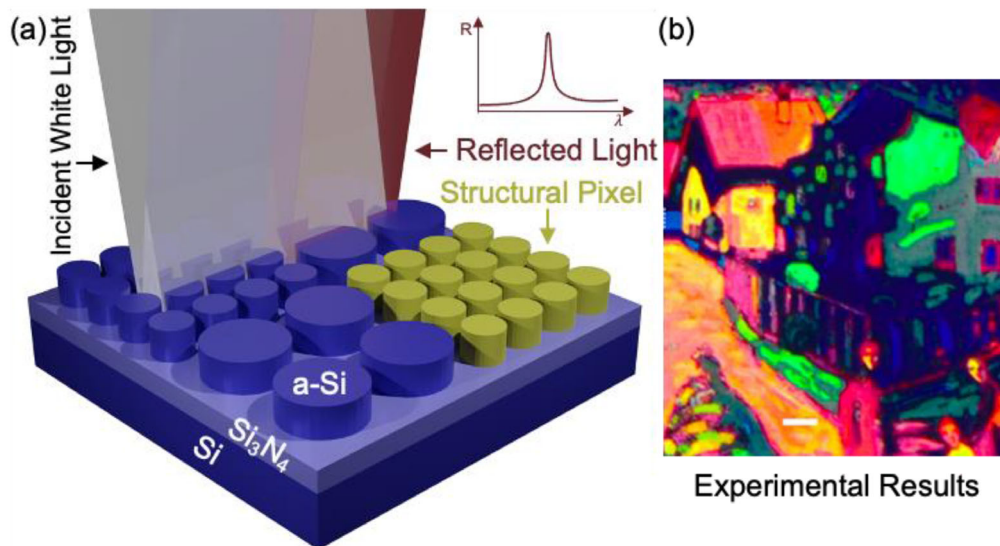


Figure 7. (a) Schematic illustration of structural color pixels. By varying the diameter and the pitch between disks one can adjust the frequencies of the reflected light. It was experimentally shown that 121% of the sRGB triangle can be covered. For that purpose, the pitch and diameter were varied in the range between ≈ 50 and 300–400 nm each.^[41] (b) Experimental results showing a reproduction of “Murnau Street with Women” by Vasily Kandinsky as seen through an optical microscope. Reproduced with permission.^[41] Copyright 2017, American Chemical Society.

3.1. Reflection/Transmission Spectrum Tuning

One of the most common applications of Mie resonances is tuning the reflection or transmission spectrum to filter out frequencies/polarizations, form images/holograms, or create a refractometer exploiting the sensitivity of resonances within a dielectric environment.^[40,41,93–98]

Mie resonators can be used both in a regular arrangement or as individual sporadically distributed elements. Structured-colors that can be created by Mie resonators can reach ultra-high resolution up to 10^5 dots per inch (DPI) – effectively bypassing the diffraction limit due to the sub-wavelength size of the resonators often made of high optical density materials such as Si. The colors in this case are being formed by selectively maximizing the back-scattering of a specific wavelength by adjusting the scatterer size.

Figure 7 shows an example of a silicon structure to form a back-reflection image. The pitch between the resonators in this experiment is as small as 250 nm, which translates into a DPI resolution exceeding 10^5 . The structure was made by etching a-Si layer deposited on a Si/Si₃N₄ stack via a mask produced by e-beam lithography. It was experimentally shown that the color space that can be covered is $\approx 121\%$ of the sRGB triangle and the colors are remaining correct for incidences of angles of up to 20 degrees. Normally, the saturation of the colors obtained by Mie-scattering are negatively impacted by the presence of a substrate due to reflections at the interface.^[41] Here, the thickness of the Si₃N₄ layer was chosen such that it could act as an antireflection coating. This makes the performance similar to one attainable by a hypothetical layer of scatterers suspended in the air. Furthermore, the demonstrated structure is CMOS-compatible which makes its production cost considerably lower than that of similar-performance plasmonic structures utilizing, e.g., silver or gold.

In a similar manner, it was demonstrated that transmission-based images with high resolution and high color-saturation can be created based on Mie-scattering.^[40] One of the promising approaches is similar to the one suggested in the previously cited paper^[41] and is based on the usage of a-Si scatterers. This time fabricated on top of a transparent glass substrate, see **Figure 8**.

The article^[40] demonstrated a large color-space that can be covered by the suggested structures as well as good match between simulation and experiment. Naturally, unlike the reflective structure, the transmitted colors are representing the inverted (subtractive) CMY (cyan-magenta-yellow) color scheme which leads to a smaller saturation of red, green, and blue colors. However, depending on the application, a transmission scheme exploiting the CMY color scheme might be more favorable than a reflection scheme exploiting the RGB colors. Mainly due to the fact that subtractive CMY colors can be stacked on top of each other by subsequent positions of the colored filters. The authors additionally mention that it should be possible to get a better RGB gamut in transmission by utilizing inverted scatterer structures.^[40]

For comparison, we also assembled a figure showing the gamut cover and shape ratio achieved by the most widely used techniques to create structural colors such as by dielectric Mie scattering, by plasmonic loss nanoparticles, by layered stacks, and nanowire structures (see **Figure 9**). The gamut represents the available color space Ω' for a given technology with respect to the full-color space Ω . In the insert of Figure 9 an example of a color gamut Ω with a triangularly covered area Ω' is shown. The covered area shows an approximation of which colors can be produced with any of the structuring techniques mentioned above. The image shows two quantities: 1) gamut cover Ω'/Ω – ratio between covered area and full area of the gamut and 2) shape ratio – equal to $(\Omega'/\partial\Omega')/(\Omega/\partial\Omega)$, where $\partial\Omega$ denotes the border length of area Ω . The latter gives a distinction between structures covering only a pencil-like shape of colors (small shape ratio values)

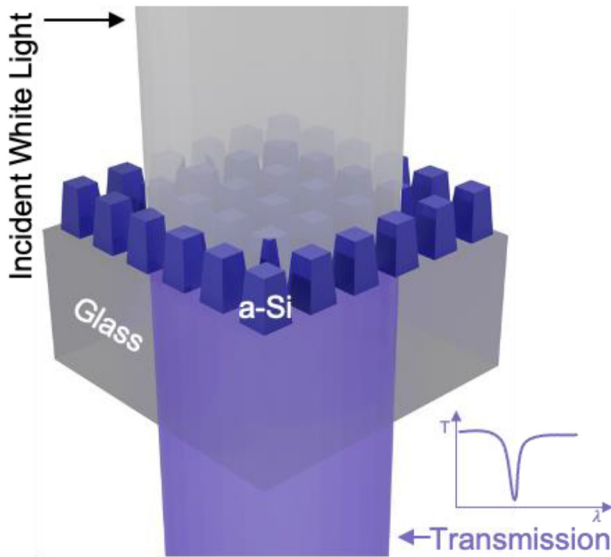


Figure 8. Schematic illustration of a-Si based transmission structural colors. By varying the period and the width of the scatterers (in the article authors use fixed width w to period p ratio of 0.6 and fixed scatterer height h of 180 nm). By changing the w/p ratio the spectrum of the transmitted light can be adjusted.^[40] The color is created in the transmission spectrum by scattering/reflecting the light around a given frequency (the color then has an inverted spectrum as schematically shown in the inset of the figure.).

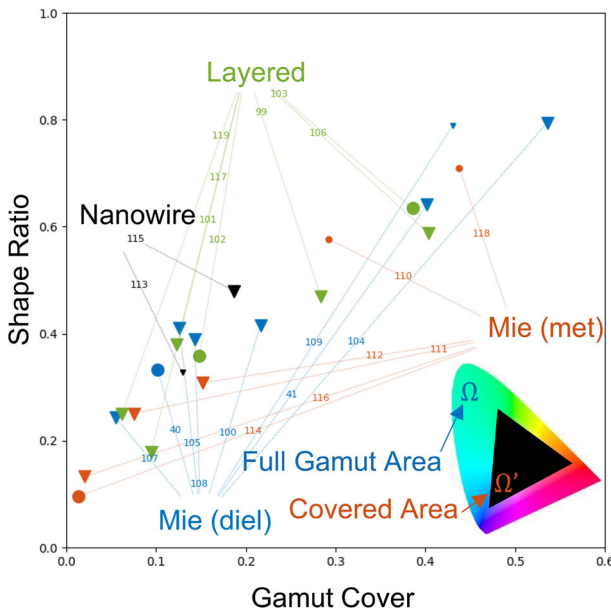


Figure 9. Comparison of gamut coverage (Ω'/Ω) and shape ratio of the covered area for layered, nanowire, and Mie-scattering (metallic and dielectric) approaches reported in recent years. The shape ratio is a ratio between area covered (Ω') and its perimeter divided by the same value for the CIE 1931 color-gamut area Ω , in other words $(\Omega'/\partial\Omega') / (\Omega/\partial\Omega)$. Triangle markers refer to reflective and circular to transmissive structures. Big markers are used for experimental results and small for theoretical.^[40,41,99–119]

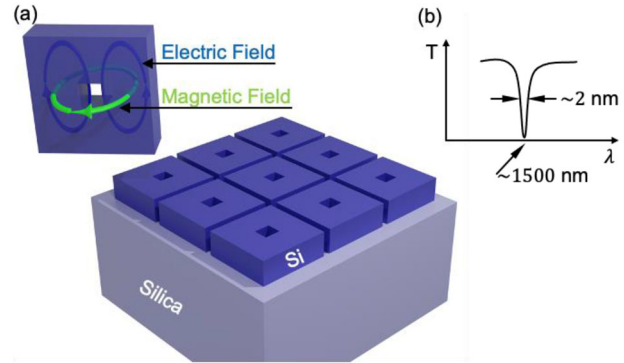


Figure 10. a) Schematic illustration of a cuboid array that supports toroidal resonances. In each cuboid, the electric field of a toroidal dipole mode is circulating in two arms of the cuboid whereas the magnetic field component is circulating around the hole in its center.^[58] b) Schematic illustration of the measured transmission. The thin absorption line corresponds to the toroidal mode with a Q-factor of 728.

and structures that extend across a large area of the color space (large shape ratio values).

In Figure 9 we divided the colors generated by Mie-scattering on dielectric and metallic to emphasize that the former are commonly based on scattering of the light while the latter on selective light absorption. Mie-based structural colors provide the best gamut cover while also having improved angular stability compared to the layered arrangements since the latter is reliant on the phase stacking between different interface reflections that are directly affected by the angle of incidence.

While the results of the gamut covered with Mie-based structural colors are impressive these structures are commonly possessing moderate Q-factors (in favor of brightness of the colors). Mie-resonators nevertheless allow obtaining much higher Q-factors if an extra effort is to be made. A special case of high-quality resonator structures are the ones employing the quasi-bound states in continuum (quasi-BiC) or anapole. Such electromagnetic oscillations are normally not-coupled to external radiation due to a specific symmetry/periodicity of the structure. The symmetry of such structures can however be broken by introducing a small asymmetry factor in the arrangement.^[48] For example, such a situation can be created by using a state that is intrinsically weakly coupled based on toroidal modes.^[58] In the geometry suggested in Ref.,^[58] see Figure 10, toroidal modes occur due to incident electric and magnetic fields that form field loops created in cuboids with a hole (see Supplementary Information, Section 5). The rectangular geometry was chosen to increase the coupling between neighboring cuboids to reach high-quality factors in order of a thousand.

Figure 10 shows the schematic illustration of the design. The cuboids are made of polycrystalline silicon deposited on a silica substrate via low-pressure chemical vapor deposition. Experimentally the quality factor of 728 was demonstrated for the wavelength of 1505 nm. The authors though point out that theoretical quality factor of similar structures can reach above two million. Additionally, an alternative material system was suggested and tested experimentally (with titania cuboids on the same substrate) and demonstrated to have quality factors of 160 at shorter wavelengths inaccessible for silicon.

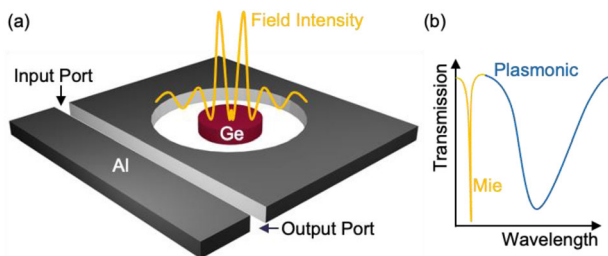


Figure 11. (a) Schematic illustration of a hybrid Mie-plasmonic modulator with a plasmonic waveguide coupled to a ring with a Ge Mie-resonator inside. The low-loss of the Mie mode allows to reach a theoretical quality factor of 1292.^[123] (b) Schematic illustration of the obtained transmission pattern as a function of the wavelength. The Mie mode has a considerably larger quality factor due to the reduced losses compared to the plasmonic mode.

3.2. Waveguiding Applications

Mie scatterers can be placed in the vicinity of waveguide-based devices to modify the spectral response. An interesting example is given here in combination with a plasmonic ring waveguide. Plasmonic ring resonators are ultra-compact and have already found interesting applications as high-performance modulators.^[120–122] However, the Q-factors of such plasmonic rings are fundamentally limited by the intrinsic losses of the metals. Yet, the Q-factor can be greatly improved by employing a Mie scatterer placed in a metallic ring-hole as suggested in,^[123] see **Figure 11**.

In this setup, an optical signal is fed from a plasmonic slot waveguide which is coupled to a plasmonic ring resonator. The transmission spectrum of the configuration is plotted in **Figure 11b**, see blue solid line. The article then suggests adding a Ge-based Mie scatterer in the form of a disk inside a metallic ring resonator. This modification, in addition to the plasmonic mode, provides a higher quality factor Mie mode that is strongly localized on the resonator. The strong localization of the mode allows to considerably reduce the losses and obtain an order of magnitude higher quality factor of the resonance when compared to the plasmonic mode in the same ring. Simulations indicated that a quality factor of 1292 could be obtainable with the structure.

Another interesting idea suggests Mie scatterers to guide an optical mode. The Mie scatterers are thereby arranged to form a waveguide. In this simulation work, it was shown that a 2D-array of infinite Ge rods waveguides can be used to guide light between just two rows of Mie resonators. The rods are positioned to strongly couple between each-other.^[124] The strong coupling creates a band-gap in the energy spectrum of the Mie-modes that can be used to efficiently contain the light in a designed volume. **Figure 12** shows the schematics of the proposed waveguide and a Y-splitter.

3.3. Photodetection and Sensing

The Mie-scattering effect can be used to create field enhancements for both narrow and broad-band light-absorption and photodetection.^[125,126] In most practical applications a single Mie-scatterer is not sufficient. For that reason, Mie-scatterers can

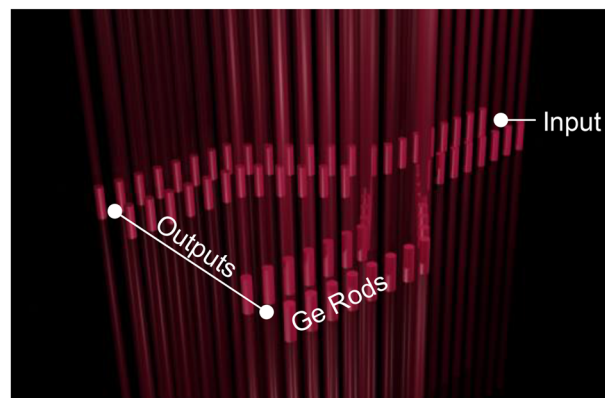


Figure 12. Schematic illustration of Y-splitter based on Ge-rod waveguides. Each waveguide line is formed by two rows of scatterers which yields theoretical splitting efficiency of 46% per arm.^[124] An important feature of the proposed design is its high tolerance to the disorder of the rod arrangement. For example, a straight waveguide with no disorder that has a transmission efficiency of 90% for a case of relatively high 10% standard deviation (normalized on the spacing between the rods) only drops down in the transmission efficiency to 75%. Authors of the article also investigated the behavior of the proposed structure in bended waveguide and power splitter configurations and found that for no disorder case, the Y-splitter gives an efficiency of 46% per arm which is on par with other splitter types such as plasmonic, photonic-crystal and topological which at the same time have either a less-compact geometry or increased power-losses.

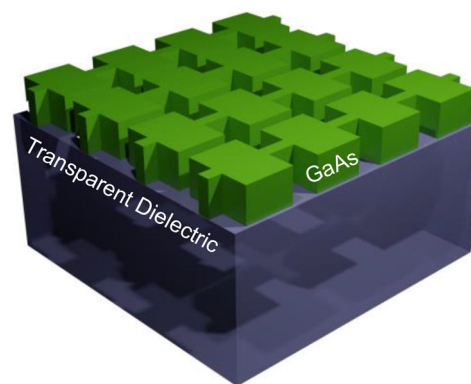


Figure 13. Schematic illustration of GaAs Mie-resonator array on a transparent substrate. It was shown that by tuning the geometrical parameters of the array one can create perfect absorption within a single resonating layer.^[68]

be used as building blocks (meta-atoms) of metamaterials and metasurfaces. The collective excitation of meta-atoms enhances the properties of a single scatter allowing for strong effects such as perfect light absorption. These effects however require multiple Mie scatterers that are still based on properties of a single scatter that can be trimmed by adjusting its geometry. Depending on the structure of a detector the Mie resonators can be placed below, above, or within an active material.^[68,125,127]

An interesting structure of a perfect absorber within a single layer of periodically arranged resonators is depicted in **Figure 13**, see^[68] By changing the geometry, the absorption band can be tuned. To create a perfect absorber two conditions are needed to be met: 1) two modes with opposite symmetries (electrical and

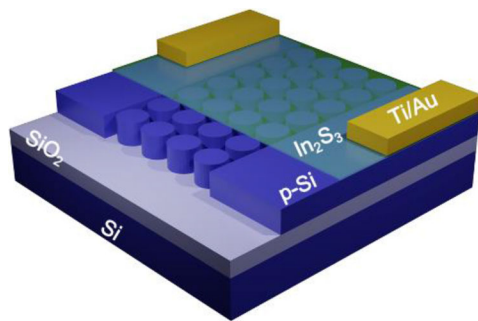


Figure 14. Schematic illustration of Mie-scattering enhanced nonlayered 2D material photodetector. An array of Si nanopillars supporting Mie-resonances is placed below the active In_2S_3 layer. The resonators enhance the absorption in the active layer and facilitate hole-trapping in Si nanopillars which are disconnected from each other and therefore suppress the dark current and create the photoconductive gain. Responsivity of 4812 A W^{-1} was measured experimentally.^[127]

magnetic dipoles) should be excited at the same frequency, 2) each of the modes needs to be critically coupled so that their radiative and non-radiative decay rates are identical. These conditions although not easily accessible can be matched by an array of Mie resonators by utilizing the electric and magnetic dipole modes that possess the desired opposite symmetry.^[128] First, the frequencies of both modes are adjusted to the same value by changing the x/y -dimensions of the central cuboids. Second, the critical coupling can be achieved by introducing a bridge between cuboids that creates a conductive channel through the structure along the incident electric field polarization and can be used to control the mode losses. To understand the requirement of having two resonances one could imagine the following. A single Mie-resonance would be inherently symmetric and would radiate in both directions away from the resonant layer. With two resonances it is possible to reach the Kerker effect when resulting radiation is directed only as forward scattering. This directed radiation under conditions of proper intensity and phase (which is satisfied by the critical coupling condition) can destructively add to the transmitted part of the incident wave in the forward direction. The latter then cancels all the field propagating away from the resonant plane creating the perfect absorption. The theoretical results were verified experimentally and good absorption (above 90%) was found at wavelengths close to 800 nm.

There are many attractive two-dimensional absorptive materials. Yet, the interaction with an external field and these materials are weak due to a small layer thickness. Detectors comprising such materials can benefit greatly from the field enhancement provided by the Mie scatterers. The prime example of 2D materials is graphene which possesses unique band-gap properties and offers high carrier mobility allowing to build detectors in an ultra-wide frequency range from infrared to UV.^[129] Another variation of 2D materials are nonlayered 2D materials (NL2D) that while not forming a separate single-atom layer can be produced as very thin films with a thickness of a few atomic periods.^[130] Such NL2D materials can possess a wide range of properties that are between 2D and 3D.^[127]

Figure 14 shows an illustration of a photodetector based on the NL2D In_2S_3 layer combined with Si nanopillars supporting Mie-modes. The Si nanopillars are produced on an SOI wafer

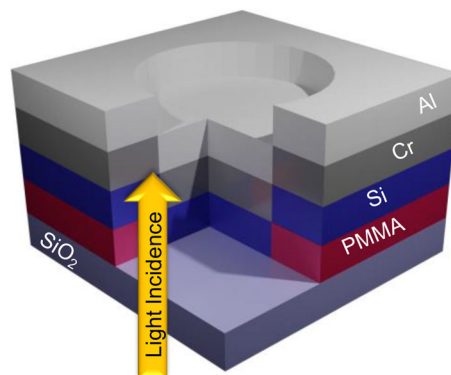


Figure 15. Schematic illustration of a triple Mie-resonance broadband absorber (designed for substrate-side illumination). The structure was shown to have an average absorption above 96% in the range between 400 and 1800 nm as well as strong angular stability up to at least 70 degrees of incidence.^[125] This absorption is reached by combining resonances occurring at the resonances of the Al, the Cr, and the Si insert layers. Individually these resonances cover only part of the target spectrum, but combined together create a strong uniform absorption.

and serve a double purpose: 1) They create a strong field enhancement that allows creating an order of magnitude stronger absorption in In_2S_3 and thereby leads to a higher carrier generation. 2) The depletion region created at the contact between the Si and In_2S_3 layer reduces the dark current (because the conductive pillars are disconnected) and creates a photoconductive gain via trapping holes in the nanopillars below the conductive layer. The detector was demonstrated to reach a high 4812 A W^{-1} responsivity at wavelength of 405 nm with a very high detectivity of $5.4 \times 10^{15} \text{ J}$. It is a promising result showing the potential of a combination of the unique properties of low-dimensional materials and electromagnetic field enhancements available via Mie-scattering.

Remarkable is, that while Mie-resonances are commonly possessing a relatively narrow spectrum (due to the resonant nature of the Mie-modes) it is possible to combine them both in lateral and vertical arrangements to achieve a broad-band absorption that can be used in detection of photovoltaics or as a filtering element.

Figure 15 shows an example of vertically stacked Mie-resonators that allow creation of a near-perfect absorption (over 96% average for normal incidence) across a wide frequency range (from 400 to 1800 nm).^[125] The structure is produced with a single lithography step on top of a silica substrate. A hole array is created by a PMMA layer deposited on top of the substrate. Subsequent evaporation steps of Si, Cr, and Al create the triple Mie-resonator structure allowing for the wide frequency range of absorption that is also angularly stable up to at least 70 degrees of incidence (at the 70 degrees benchmark the average absorption value only drops down to $\approx 85\%$). Remarkably in the suggested design the total thickness of all the structured layers is below 300 nm which makes it flexible in terms of potential applications for detection, imaging, or photovoltaic applications.

3.4. Photoemission and Lasing

Another area to use Mie-scatterers applications relates to the enhancement of photoemission, the high-harmonic generation,

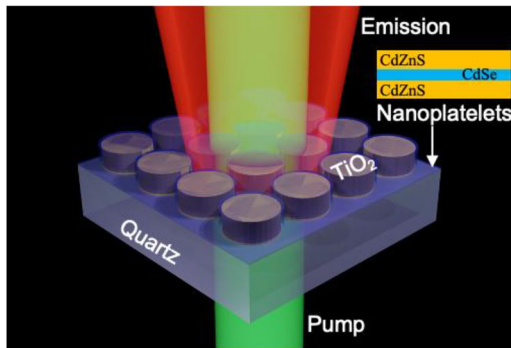


Figure 16. Schematic illustration of laser emission enhancement for an optically pumped thin film of colloidal nanoplatelets coupled to an array of Mie-scatterers. It was demonstrated that the structure offers a low lasing threshold of $\approx 40 \mu\text{J cm}^{-2}$ under room temperature operation.^[51]

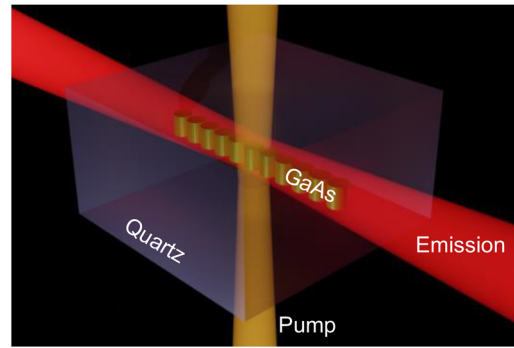


Figure 17. Schematic illustration of 1D Mie-scatterer array cavity for optically pumped laser. Quasi-BiC mode of the array was utilized to achieve lasing with $5 \mu\text{J cm}^{-2}$ threshold and mode Q-factor of 1010 at temperature of 77K.^[53]

and or even the lasing. Mie-modes can be utilized to increase the local photon state density for more efficient photoemission (Purcell effect), and create laser cavities and high-quality-factor resonators for high harmonic generation. It was shown, for example, that by utilizing field enhancement created by Si sphere, quadrupole modes together with Auger effect enhanced by dipole modes (that increases the nonradiative lifetime of the carriers). It has already been shown that five orders of magnitude increased photoluminescence from Si nanospheres in comparison to bulk Si can be achieved.^[54]

Figure 16 shows an example of a structure where a Mie-resonator array was utilized to create lasing at room temperature from a thin film of colloidal CdZnS/CdSe nanoplatelets. An array of TiO_2 on a transparent quartz substrate was covered by nanoplatelets. Here, these quantum wells were comprised of a few atomic layers thick CdSe between two CdZnS shell-layers deposited from solution on top of the Mie-scatterer array.^[51]

Remarkable results were achieved in terms of the low lasing threshold of $\approx 40 \mu\text{J cm}^{-2}$ at room temperature. The wavelengths of the laser emission were also demonstrated to be adjustable by varying the Mie-resonance frequency via changing the size of the scatterers. A Q-factor of 2590 was reached in the experiment at the lasing wavelength $\approx 650 \text{ nm}$. That high-quality factor is associated with a quasi-BiC mode that is supported by the periodic array of scatterers.

Similarly to the previous example, Mie-scatterers can be used in 1D arrangement to create laser cavities.^[53] An advantage for applications such as photonic integrated circuits is the lateral radiation that can be easily coupled into a waveguide. One of the common solutions for such lasers are horizontally oriented nanowires. However, the authors of the article demonstrated theoretically and experimentally that a cavity composed of a hundred cylindrical Mie-scatters made of GaAs outperforms a nanowire of corresponding size by an order of magnitude in the lasing intensity.

Figure 17 shows the schematic illustration of the design studied.^[53] A thin GaAs layer was transformed onto a quartz substrate with subsequent etching of the nanopillar array. An HSQ cover of $2 \mu\text{m}$ was subsequently deposited to surround the Mie-scatterer cavity with a media of uniform permittivity. The lasing

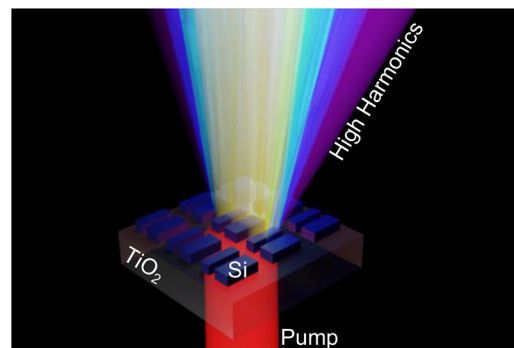


Figure 18. Schematic illustration of high-harmonic generation using controlled asymmetry in an array of Si Mie-scatterers on titania substrate. The generation up to the 11th harmonic was observed experimentally.^[48]

was detected in a cryogenic setup under temperature of 77K. It was found that the lasing mode has a Q-factor of 1010 and a lasing threshold of $5 \mu\text{J cm}^{-2}$. As pointed out by the authors such a design is beneficial for integrated photonic applications due to its natural compatibility with the waveguide coupling. Moreover, it was shown theoretically and experimentally that asymmetric excitation of the array can lead to a unidirectional lasing that removes the necessity to handle the backward beam appearing in case of symmetric or uniform excitations.

The high Q-factor of the quasi-BiC modes can also be used to enhance the high harmonic generation. For that purpose, a structure was suggested that allows tuning the ratio between radiative and non-radiative decay of a BiC mode to reach the condition of critical coupling and maximize the field enhancement.^[48]

Figure 18 shows a schematic illustration of the proposed design. An array of Si nanoblocks is placed on top of a TiO_2 substrate. The nanoblocks are placed in pairs and one of them is reduced in thickness compared to the other. That reduction allows controlling the coupling between the quasi-BiC modes in the array and the external radiation. By adjusting this factor to reach the critical coupling condition one can then maximize the field enhancement and the high-harmonic generation. Generation of up to the 11th harmonic of a laser at a wavelength $\approx 3800 \text{ nm}$ was demonstrated experimentally.^[48]

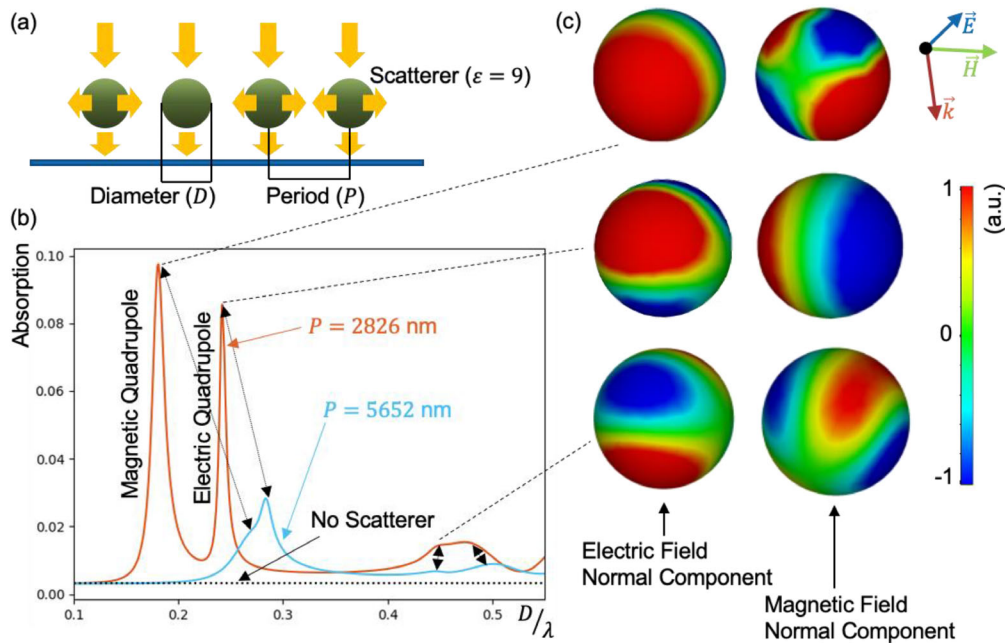


Figure 19. a) Mie resonators (green) placed above a weakly absorbing layer (blue line). b) Absorption in the weakly absorbing layer in dependence on the diameter-to-wavelength ratio of the scatterer. c) To the right, we have depicted the normal components of the electric and magnetic field for three selected peaks from the absorption graph. The pattern observed for the normal component of the fields shows which modes are dominant among the electric and magnetic subsets. For instance, the first resonance emerges at $D/\lambda = 0.18$. The plots show electric dipole and magnetic quadrupole resonances. However, only the quadrupole mode has a significant scattering within the surface. For that reason, we associate the absorption peak with the magnetic quadrupole.

4. Absorption Enhancement by Generation of an In-plane Propagating Mode

Here, we demonstrate how the proper choice of Mie scatterer dimensions and arrangement of the scatterers can be used to generate a dominant in-plane scattering. This can then be used to boost the absorption in a thin later layer.

Toward this end, we consider a simple periodic arrangement of spherical particles of permittivity $\epsilon = 9$ in the air. **Figure 19** shows schematics of the structure. Beneath the scatterers, there is a thin (10 nm) weakly absorbing ($\epsilon = 1.0 + 0.1j$) layer. By means of frequency-domain numerical simulations, we can observe the behavior of the absorption in the layer in dependence on the scatterer diameter-to-wavelength ratio. For the simulation purposes, we used a wavelength of 2 μm , however, it is worth noting that in the absence of material dispersion, the mode amplitudes do not depend on the scatterer size, and the wavelength only changes with their ratio. The CST Microwave Studio software package was used for the full-wave simulations below.

In **Figure 19** one can see the dependence of the absorption when varying wavelength while keeping the periodicity $P = 2826$ and 5652 nm. One can see two very pronounced absorption peaks of almost 10% around $D/\lambda = 0.18$ and 8.5% around $D/\lambda = 0.24$. These are substantial absorptions for such a thin layer with a weak absorptivity. The high absorptivity can be understood by a study of the normal field components on the surface of the scatterers (see **Figure 19c**). Each time when the absorption is large, either electric or magnetic field components (or both) show the

dominance of a corresponding quadrupole mode. These modes have a large lateral-scattering pattern (see **Figure 3**).

The first-period value P was obtained by optimizing the parameters such as particle size, distance to the absorbing layer, and the period (optimization was done for the maximal absorption in the thin layer for the strongest peak found). The second value was subsequently chosen to be twice bigger (to keep the phase relation between scattered fields of neighboring particles) to observe the peak behavior with decreasing scatterer density. One can see that even in the case of very sparsely placed scatterers a considerable absorption enhancement can be observed. If we compare the absorption that we observe with and without the scatterers we find that we have ≈ 30 times increase in the absorption. This increase can be utilized to boost absorption in weakly absorbing 2D layers or even small-scale photodetectors placed in the vicinity of the scatterers.

As a remark, to tell as of which Mie modes are dominant for a specific absorption resonance one has to study the fields normal to the surface. By looking at the pattern of normal field components at the surface, one can tell which modes are dominant among the electric and magnetic subsets. This statement stems from the theoretical discussion in the introduction (see **Figure 2** and Equation (1.3), where one can see that only the source fields \vec{S} have an \vec{z}_r component). From this equation one can see that only electric modes have electric field components normal to the surface of a scatterer. Likewise, only magnetic modes have magnetic field components normal to the surface of scatterer. As such, a solid understanding of the scattering patterns of the

modes allows one to manipulate the light in a way such that it can effectively couple to nano-scale layers as shown in the example above. One may think of many more examples where light scattering and manipulation using Mie modes can trigger new applications for guiding, imaging, and sensing.

5. Conclusion

The Mie-scattering can be used in a variety of ways to boost the performance of photonic devices and structures by giving control over the reflection, transmission, diffraction, and absorption spectrum as well as the light polarization. It can be used to create structural images and holograms, chemical sensors, boost photodetector performance, design topological waveguides, and multiple other applications where light management with low optical losses is required.

Notably, the Mie-scattering modes do not rely on the strict ordering of the scatterers to achieve a desired effect and as such are compatible with cheap and easily-scalable solution processing techniques to distribute/include nanoparticles over/into photonic and photoelectronic devices and structures. At the same time due to the large variety of available materials, Mie scattering allows depositing scatterers within existing widely used stacks such as SOI-wafers and to deposit them with scalable lithography techniques such as nanoimprint.

In this article, we present a summary of the Mie theory, the properties of the Mie-scattering modes, and their behavior in metal and dielectric particles. We show how metallic particles are mostly supporting electric multipole modes in the sub-wavelength regime (due to the high conductivity) while in dielectric particles both electric and magnetic modes are excited. Furthermore, we show metallic particles in a deep sub-wavelength regime with strong plasmonic absorption that is unique to metallic particles. We further analyze the mode amplitude behavior and show how Mie modes can control the direction of scattered light leading to phenomena such as the Kerker effect. We also discuss special types of modes such as non-radiative modes or anapoles and show how they appear in the solution of the Maxwell equations (see Supplementary Information, Section 5).

The paper ends with a proposal to exploit the directivity of scattering created by higher-order modes such as quadrupoles to reach considerable enhancements in the absorption of a thin-layer material situated along the scattering plane.

We believe that with further advances in processing techniques, more and more applications exploiting Mie-resonance structures will become commercially feasible. Structured colors that are already applied to some extent, for example, in automobile industry are robust against degradation by UV light and provide vivid visual effects that can also be adjusted based on the viewing angle. Further development of processing technologies such as nano-imprint and Talbot lithography will allow to extend the availability of structural colors based on Mie scattering in many more application areas. Mie modes, besides scattering of light, can also be guided and utilized in resonator cavities. Mie resonators often seem to demonstrate robustness against processing inaccuracies. A most interesting application area includes the ability of Mie modes to enhance light-matter interaction. This may have a strong impact on applications that encompass low-dimensional materials and nano-scaled structures.

This is of interest to create more compact and efficient detectors and sensors. Additionally, strong light-matter interaction allows to intensify high-harmonic generations that can be used to create ultra-short pulses or extreme UV-radiation sources.

Supporting Information

Supporting Information is available from the Wiley Online Library or from the author.

Acknowledgements

Open access funding provided by Eidgenössische Technische Hochschule Zurich.

Conflict of Interest

The authors declare no conflict of interest.

Keywords

metamaterials, metasurfaces, Mie-scattering, nanostructures, plasmonics

Received: January 18, 2023

Revised: June 11, 2023

Published online: July 21, 2023

- [1] S. Daqiqeh Rezaei, Z. Dong, J. You En Chan, J. Trisno, R. J. H. Ng, Q. Ruan, C.-W. Qiu, N. A. Mortensen, J. K. W. Yang, *ACS Photonics* **2021**, *8*, 18.
- [2] K. Koshelev, Y. Kivshar, *ACS Photonics* **2021**, *8*, 102.
- [3] P. C. Wu, et al., *Nat. Commun.* **2019**, *10*, 9.
- [4] K. Wang, Y. Xiong, Q. Li, Y. Wang, J. Zhang, H. Liu, Z. Liu, T. Wang, Z. Shen, X. Wang, X. Wang, J. Gao, H. Yang, *Opt. Express* **2022**, *30*, 22830.
- [5] X. Pan, H. Wang, D. Zhang, S. Xun, M. Ouyang, W. Fan, Y. Guo, Y. Wu, S. Huang, K. Bi, M. Lei, *PLoS One* **2016**, *11*, 8.
- [6] M. C. Tsai, T. L. Tsai, C. T. Lin, R. J. Chung, H. S. Sheu, H. T. Chiu, C. Y. Lee, *J. Phys. Chem. C* **2008**, *112*, 2697.
- [7] T. Badloe, et al., *Light: Sci. Appl.* **2022**, *11*, 118.
- [8] I.-C. Bena-Chelms, Y. Salamin, F. F. Settembrini, Y. Fedoryshyn, W. Heni, D. L. Elder, L. R. Dalton, J. Leuthold, J. Faist, *Optica* **2020**, *7*, 498.
- [9] Y. Salamin, I.-C. Bena-Chelms, Y. Fedoryshyn, W. Heni, D. L. Elder, L. R. Dalton, J. Faist, J. Leuthold, *Nat. Commun.* **2019**, *10*, 5550.
- [10] M. L. Solomon, J. Hu, M. Lawrence, A. García-Etxarri, J. A. Dionne, *ACS Photonics* **2019**, *6*, 43.
- [11] X. Fu, Q. Wang, J. Wang, Z. Huang, X. Li, D. Wen, J. Fang, B. Li, S. Zhou, H. Zhang, *J. Mater. Chem. C* **2021**, *9*, 13704.
- [12] O. Mitrofanov, et al., *APL Photonics* **2018**, *3*, 6.
- [13] Z. Yuan, P. C. Wu, Y.-C. Chen, *Laser Photonics Rev.* **2022**, *16*, 2100202.
- [14] S. Sun, et al., *Laser Photonics Rev.* **2023**, *n/a*, 2200814.
- [15] I. Staude, T. Pertsch, Y. S. Kivshar, *ACS Photonics* **2019**, *6*, 802.
- [16] B. Sain, C. Meier, T. Zentgraf, *Advanced Photonics* **2019**, *1*, 024002.
- [17] L. Carletti, K. Koshelev, C. De Angelis, Y. Kivshar, *Phys. Rev. Lett.* **2018**, *121*, 5.
- [18] K. Frizyuk, I. Volkovskaya, D. Smirnova, A. Poddubny, M. Petrov, *Phys. Rev. B* **2019**, *99*, 15.

- [19] E. V. Melik-Gaykazyan, S. S. Kruk, R. Camacho-Morales, L. Xu, M. Rahmani, K. Zangeneh Kamali, A. Lamprianidis, A. E. Miroshnichenko, A. A. Fedyanin, D. N. Neshev, Y. S. Kivshar, *ACS Photonics* **2018**, *5*, 728.
- [20] F. Timpu, A. Sergeyev, N. R. Hendricks, R. Grange, *ACS Photonics* **2017**, *4*, 76.
- [21] A. G. F. De Beer, S. Roke, *Phys. Rev. B* **2009**, *79*, 9.
- [22] G. Mie, *Ann. Phys.-Berlin* **1908**, *330*, 377.
- [23] E. Mikheeva, J.-B. Claude, M. Salomoni, J. Wenger, J. Lumeau, R. Abdeddaim, A. Ficorella, A. Gola, G. Paternoster, M. Paganoni, E. Auffray, P. Lecoq, S. Enoch, *APL Photonics* **2020**, *5*, 116105.
- [24] D. I. Vulis, Y. Li, O. Reshef, P. Camayd-Muñoz, M. Yin, S. Kita, M. Lončar, E. Mazur, *Opt. Express* **2017**, *25*, 12381.
- [25] B. Wang, Y. Xu, Z. Wu, Z. Zhang, Q. Wang, *Opt. Commun.* **2023**, *540*, 129485.
- [26] S. Venkatesh, X. Lu, H. Saeidi, K. Sengupta, *Nat. Electron.* **2020**, *3*, 785.
- [27] N. Li, Z. Xu, Y. Dong, T. Hu, Q. Zhong, Y. H. Fu, S. Zhu, N. Singh, *Nanophotonics* **2020**, *9*, 3071.
- [28] Z. Xu, Y. Dong, C.-K. Tseng, T. Hu, J. Tong, Q. Zhong, N. Li, L. Sim, K. H. Lai, Y. Lin, D. Li, Y. Li, V. Bliznetsov, Y.-H. Fu, S. Zhu, Q. Lin, D. H. Zhang, Y. Gu, N. Singh, D.-L. Kwong, *Opt. Express* **2019**, *27*, 26060.
- [29] P.-M. Coulon, et al., *Microsyst. Nanoeng.* **2019**, *5*, 52.
- [30] H. H. Solak, C. Dais, F. Clube, *Opt. Express* **2011**, *19*, 10686.
- [31] L. Stuerzebecher, T. Harzendorf, U. Vogler, U. D. Zeitner, R. Voelkel, *Opt. Express* **2010**, *18*, 19485.
- [32] A. Isoyan, F. Jiang, Y. C. Cheng, F. Cerrina, P. Wachulak, L. Urbanski, J. Rocca, C. Menoni, M. Marconi, *J. Vac. Sci. Technol. B* **2009**, *27*, 2931.
- [33] A. A. Bushunov, M. K. Tarabrin, V. A. Lazarev, *Laser Photonics Rev.* **2021**, *15*, 2000202.
- [34] H. Sugimoto, T. Okazaki, M. Fujii, *Adv. Opt. Mater.* **2020**, *8*, 2000033.
- [35] Y. Wu, Y. Chen, Q. Song, S. Xiao, *Adv. Opt. Mater.* **2021**, *9*, 2002126.
- [36] A. A. Basharin, V. Chuguevsky, N. Volsky, M. Kafesaki, E. N. Economou, *Phys. Rev. B* **2017**, *95*, 035104.
- [37] I. Kim, G. Yoon, J. Jang, P. Genevet, K. T. Nam, J. Rho, *ACS Photonics* **2018**, *5*, 3876.
- [38] C. Ji, K.-T. Lee, T. Xu, J. Zhou, H. J. Park, L. J. Guo, *Adv. Opt. Mater.* **2017**, *5*, 1700368.
- [39] X. Y. He, F. T. Lin, F. Liu, W. Z. Shi, *J. Phys. D-Appl. Phys.* **2020**, *53*, 9.
- [40] T. Lee, J. Kim, I. Koirala, Y. Yang, T. Badloe, J. Jang, J. Rho, *ACS Appl. Mater. Interfaces* **2021**, *13*, 26299.
- [41] Z. Dong, J. Ho, Y. F. Yu, Y. H. Fu, R. Paniagua-Dominguez, S. Wang, A. I. Kuznetsov, J. K. W. Yang, *Nano Lett.* **2017**, *17*, 7620.
- [42] A. Komar, R. A. Aoni, L. Xu, M. Rahmani, A. E. Miroshnichenko, D. N. Neshev, *ACS Photonics* **2021**, *8*, 864.
- [43] J. Hu, M. Lawrence, J. A. Dionne, *ACS Photonics* **2020**, *7*, 36.
- [44] A. Dorodnyy, Y. Salamin, P. Ma, J. Vukajlovic Plestina, N. Lassaline, D. Mikulic, P. Romero-Gomez, A. Fontcuberta I Morral, J. Leuthold, *IEEE J. Sel. Top. Quantum Electron.* **2018**, *24*, 1.
- [45] P. Ma, Y. Salamin, B. Baeuerle, A. Josten, W. Heni, A. Emboras, J. Leuthold, *ACS Photonics* **2019**, *6*, 154.
- [46] L. Ohnoutek, J.-Y. Kim, J. Lu, B. J. Olohan, D. M. Rasadean, G. Dan Panto?, N. A. Kotov, V. K. Valev, *Nat. Photonics* **2022**, *16*, 126.
- [47] K.-T. Lee, M. Taghinejad, J. Yan, A. S. Kim, L. Raju, D. K. Brown, W. Cai, *ACS Photonics* **2019**, *6*, 2663.
- [48] G. Zograf, K. Koshelev, A. Zalogina, V. Korolev, R. Hollinger, D.-Y. Choi, M. Zuercher, C. Spielmann, B. Luther-Davies, D. Kartashov, S. V. Makarov, S. S. Kruk, Y. Kivshar, *ACS Photonics* **2022**, *9*, 567.
- [49] T. Veeken, B. Daiber, H. Agrawal, M. Aarts, E. Alarcón-Lladó, E. C. Garnett, B. Ehrler, J. Van De Groep, A. Polman, *Nanoscale Adv* **2022**, *4*, 1088.
- [50] S. Chen, L. Li, F. Jin, C. Lu, S. Zhao, J. Niu, L. Shi, *Opt. Laser Technol.* **2022**, *148*, 107762.
- [51] M. Wu, S. T. Ha, S. Shendre, E. G. Durmusoglu, W.-K. Koh, D. R. Abujetas, J. A. Sánchez-Gil, R. Paniagua-Dominguez, H. V. Demir, A. I. Kuznetsov, *Nano Lett.* **2020**, *20*, 6005.
- [52] Y. Z. Hu, H. G. Li, Y. Zhang, Y. G. Zhu, Y. Yang, *Phys. Rev. B* **2020**, *102*, 9.
- [53] T. X. Hoang, S. T. Ha, Z. Pan, W. K. Phua, R. Paniagua-Dominguez, C. E. Png, H.-S. Chu, A. I. Kuznetsov, *Nano Lett.* **2020**, *20*, 5655.
- [54] C. Y. Zhang, et al., *Nat. Commun.* **2018**, *9*, 7.
- [55] K. Koshelev, G. Favraud, A. Bogdanov, Y. Kivshar, A. Fratallocchi, *Nanophotonics* **2019**, *8*, 725.
- [56] G.-D. Liu, X. Zhai, S.-X. Xia, Qi Lin, C.-J. Zhao, L.-L. Wang, *Opt. Express* **2017**, *25*, 26045.
- [57] A. A. Basharin, M. Kafesaki, E. N. Economou, C. M. Soukoulis, V. A. Fedotov, V. Savinov, N. I. Zheludev, *Phys. Rev. X* **2015**, *5*, 011036.
- [58] J. Jeong, M. D. Goldflam, S. Campione, J. L. Briscoe, P. P. Vabishchevich, J. Nogan, M. B. Sinclair, T. S. Luk, I. Brener, *ACS Photonics* **2020**, *7*, 1699.
- [59] E. A. Gurvitz, K. S. Ladutenko, P. A. Dergachev, A. B. Evlyukhin, A. E. Miroshnichenko, A. S. Shalin, *Laser Photonics Rev.* **2019**, *13*, 1800266.
- [60] A. E. Miroshnichenko, A. B. Evlyukhin, Y. F. Yu, R. M. Bakker, A. Chipouline, A. I. Kuznetsov, B. Luk'yanchuk, B. N. Chichkov, Y. S. Kivshar, *Nat. Commun.* **2015**, *6*, 8069.
- [61] A. Ahmadvand, B. Gerislioglu, R. Ahuja, Y. K. Mishra, *Laser Photonics Rev.* **2020**, *14*, 1900326.
- [62] C. W. Hsu, B. Zhen, A. D. Stone, J. D. Joannopoulos, M. Soljacic, *Nat. Rev. Mater.* **2016**, *1*, 16048.
- [63] N. Talebi, S. Guo, P. A. v. Aken, *Nanophotonics* **2018**, *7*, 93.
- [64] B. Luk'yanchuk, R. Paniagua-Dominguez, A. I. Kuznetsov, A. E. Miroshnichenko, Y. S. Kivshar, *Philos. Trans. R. Soc., A* **2017**, *375*, 20160069.
- [65] B. Luk'yanchuk, R. Paniagua-Dominguez, A. I. Kuznetsov, A. E. Miroshnichenko, Y. S. Kivshar, *Phys. Rev. A* **2017**, *95*, 063820.
- [66] E. E. Radescu, G. Vaman, *Phys. Rev. E* **2002**, *65*, 046609.
- [67] S. E. Svyakhovskiy, V. V. Ternovskiy, M. I. Tribelsky, *Opt. Express* **2019**, *27*, 23894.
- [68] O. Mitrofanov, et al., *APL Photonics* **2020**, *5*, 101304.
- [69] A. Cardin, K. Fan, W. Padilla, *Opt. Express* **2018**, *26*, 17669.
- [70] J. R. Piper, V. Liu, S. Fan, *Appl. Phys. Lett.* **2014**, *104*, 251110.
- [71] A. E. Miroshnichenko, M. I. Tribelsky, *Phys. Rev. Lett.* **2018**, *120*, 033902.
- [72] O. D. Miller, A. G. Polimeridis, M. T. Homer Reid, C. W. Hsu, B. G. Delacy, J. D. Joannopoulos, M. Soljacic, S. G. Johnson, *Opt. Express* **2016**, *24*, 3329.
- [73] J.-P. Hugonin, M. Besbes, P. Ben-Abdallah, *Phys. Rev. B* **2015**, *91*, 180202.
- [74] L. L. Hale, P. P. Vabishchevich, T. Siday, C. T. Harris, T. S. Luk, S. J. Addamane, J. L. Reno, I. Brener, O. Mitrofanov, *Opt. Express* **2020**, *28*, 35284.
- [75] M. I. Tribelsky, A. E. Miroshnichenko, *Phys. Rev. A* **2019**, *100*, 053824.
- [76] M. I. Tribelsky, J.-M. Geffrin, A. Litman, C. Eyraud, F. Moreno, *Phys. Rev. B* **2016**, *94*, 121110.
- [77] E. Kamenetskii, A. Sadreev, A. Miroshnichenko, *Fano Resonances in Optics and Microwaves*, Springer, Amsterdam **2018**.
- [78] S. V. Boriskina, N. I. Zheludev, *Singular and Chiral Nanoplasmonics*, CRC Press, Boca Raton, FL, USA **2015**.
- [79] B. Luk'yanchuk, N. I. Zheludev, S. A. Maier, N. J. Halas, P. Nordlander, H. Giessen, C. T. Chong, *Nat. Mater.* **2010**, *9*, 707.
- [80] B. Zhen, S.-L. Chua, J. Lee, A. W. Rodriguez, X. Liang, S. G. Johnson, J. D. Joannopoulos, M. Soljacic, O. Shapira, *Proc. Natl. Acad. Sci. USA* **2013**, *110*, 13711.
- [81] C. Wu, A. B. Khanikaev, G. Shvets, *Phys. Rev. Lett.* **2011**, *106*, 4.
- [82] M. Masharin, et al., arXiv preprint arXiv:2305.12973 **2023**.
- [83] C. F. Bohren, D. R. Huffman, *Absorption and Scattering of Light by Small Particles*. **1983**, Ch. 4.

- [84] É. Sakat, A. Moreau, J.-P. Hugonin, *Phys. Rev. B* **2021**, *103*, 235422.
- [85] M. Moaied, K. Ostrikov, S. Palomba, *Plasmonics* **2021**, *16*, 1261.
- [86] M. Kupresak, X. Zheng, G. A. E. Vandenbosch, V. V. Moshchalkov, *Advanced Theory and Simulations* **2018**, *1*, 1800076.
- [87] A. Dorodnyy, S. M. Koepfli, A. Lochbaum, J. Leuthold, *Sci. Rep.* **2020**, *10*, 17941.
- [88] N. Dordevic, R. Schwanninger, M. Yarema, S. Koepfli, O. Yarema, Y. Salamin, N. Lassaline, B. Cheng, N. Yazdani, A. Dorodnyy, Y. M. Fedoryshyn, V. Wood, J. Leuthold, *ACS Photonics* **2022**, *9*, 482.
- [89] Y. Salamin, B. Baeuerle, W. Heni, F. C. Abrecht, A. Josten, Y. Fedoryshyn, C. Haffner, R. Bonjour, T. Watanabe, M. Burla, D. L. Elder, L. R. Dalton, J. Leuthold, *Nat. Photonics* **2018**, *12*, 749.
- [90] I. Brener, S. Liu, I. Staude, J. Valentine, C. Holloway, *Dielectric Metamaterials: Fundamentals, Designs, and Applications*, Woodhead Publishing, Cambridge, UK **2019**
- [91] B. S. Luk'yanchuk, R. Paniagua-Domínguez, I. Minin, O. Minin, Z. Wang, *Opt. Mater. Express* **2017**, *7*, 1820.
- [92] S. Shen, Z. Ruan, S. Li, Y. Yuan, H. Tan, *Results in Physics* **2021**, *23*, 104057.
- [93] W. Dandan, J. C. Jasper, M. Jiajun, B. C. Kenneth, *Advanced Photonics* **2021**, *3*, 024001.
- [94] J. Meng, J. J. Cadusch, K. B. Crozier, *Nano Lett.* **2020**, *20*, 320.
- [95] Z. Liu, Q. Cui, Z. Huang, L. J. Guo, *ACS Photonics* **2020**, *7*, 1418.
- [96] S.-C. Yang, K. Richter, W.-J. Fischer, *Appl. Phys. Lett.* **2015**, *106*, 081112.
- [97] W. He, W. Zhang, J. Zhang, P. Yu, P. Liu, G. Yang, H. Lei, *Appl. Phys. Lett.* **2021**, *119*, 7.
- [98] Y. Han, Z. Meng, Y. Wu, S. Zhang, S. Wu, *ACS Appl. Mater. Interfaces* **2021**, *13*, 57796.
- [99] H. Wang, L. J. Guo, *iScience* **2022**, *25*, 104339.
- [100] C. Jung, Y. Yang, J. Jang, T. Badloe, T. Lee, J. Mun, S.-W. Moon, J. Rho, *Nanophotonics* **2021**, *10*, 919.
- [101] Z. Yang, C. Ji, Q. Cui, L. J. Guo, *Adv. Opt. Mater.* **2020**, *8*, 2000317.
- [102] I. Kim, J. Yun, T. Badloe, H. Park, T. Seo, Y. Yang, J. Kim, Y. Chung, J. Rho, *Photonics Res* **2020**, *8*, 1409.
- [103] J. Jang, K. Kang, N. Raeis-Hosseini, A. Ismukhanova, H. Jeong, C. Jung, B. Kim, J.-Y. Lee, I. Park, J. Rho, *Adv. Opt. Mater.* **2020**, *8*, 1901932.
- [104] J. Jang, T. Badloe, Y. Yang, T. Lee, J. Mun, J. Rho, *ACS Nano* **2020**, *14*, 15317.
- [105] J. Jang, T. Badloe, Y. C. Sim, Y. Yang, J. Mun, T. Lee, Y.-H. Cho, J. Rho, *Nanoscale* **2020**, *12*, 21392.
- [106] Z. Yang, C. Ji, D. Liu, L. J. Guo, *Adv. Opt. Mater.* **2019**, *7*, 1900739.
- [107] S.-Q. Li, W. Song, M. Ye, K. B. Crozier, *ACS Photonics* **2018**, *5*, 2374.
- [108] T. Wood, M. Naffouti, J. Berthelot, T. David, J.-B. Claude, L. Métayer, A. Delobbe, L. Favre, A. Ronda, I. Berbezier, N. Bonod, M. Abbarchi, *ACS Photonics* **2017**, *4*, 873.
- [109] V. Vashistha, G. Vaidya, R. S. Hegde, A. E. Serebryannikov, N. Bonod, M. Krawczyk, *ACS Photonics* **2017**, *4*, 1076.
- [110] Y. Wen, J. Lin, K. Chen, Y.-S. Lin, B.-R. Yang, *Opt. Laser Technol.* **2022**, *150*, 108004.
- [111] H. Wang, L. Huang, Y. Zhang, Y. Cai, L. Cheng, L. Zhai, Y. Liu, X. Zhang, J. Zhu, *Opt. Mater. Express* **2022**, *12*, 2270.
- [112] P. F. Lyu, T. Gong, M. R. S. Dias, M. S. Leite, *Adv. Opt. Mater.* **2022**, *10*, 6.
- [113] R. Kohandani, S. S. Saini, *Plasmonics* **2022**, *17*, 1549.
- [114] J. Y. Kim, H. J. Cho, Y. S. Do, *Nanomaterials* **2022**, *12*, 11.
- [115] Y. Huang, F. Lv, J. Chen, S. He, Z. Wang, J. La, D. Wu, R. Cong, Y. Wang, W. Wang, *Nanotechnology* **2022**, *33*, 8.
- [116] J. C. Blake, S. Rossi, M. P. Jonsson, A. Dahlin, *Adv. Opt. Mater.* **2022**, *10*, 2200471.
- [117] Q. Hu, K.-T. Lin, H. Lin, Y. Zhang, B. Jia, *ACS Nano* **2021**, *15*, 8930.
- [118] J. Gu, Y. Zhang, Y. Miao, X. Lu, X. Gao, *Opt. Commun.* **2021**, *496*, 127127.
- [119] S. Chen, S. Rossi, R. Shanker, G. Cincotti, S. Gamage, P. Kühne, V. Stanishev, I. Engquist, M. Berggren, J. Edberg, V. Darackchieva, M. P. Jonsson, *Adv. Mater.* **2021**, *33*, 2170261.
- [120] M. Burla, C. Hoessbacher, W. Heni, C. Haffner, Y. Fedoryshyn, D. Werner, T. Watanabe, H. Massler, D. L. Elder, L. R. Dalton, J. Leuthold, *APL Photonics* **2019**, *4*, 056106.
- [121] P. Ma, et al., in *European Conference on Optical Communication (ECOC)*, (Eds: J. Harder, C. Offrein, B. Leuthold, H. Limberger), Optica Publishing Group, Washington DC, USA **2022**.
- [122] C. Haffner, D. Chelladurai, Y. Fedoryshyn, A. Josten, B. Baeuerle, W. Heni, T. Watanabe, T. Cui, B. Cheng, S. Saha, D. L. Elder, L. R. Dalton, A. Boltasseva, V. M. Shalaev, N. Kinsey, J. Leuthold, *Nature* **2018**, *556*, 483.
- [123] D. Yao, Y. Zhang, Y. Huang, Y. Liu, G. Han, Y. Hao, *IEEE Photonics J.* **2021**, *13*, 1.
- [124] K. Goudarzi, *Opt. Express* **2021**, *29*, 32951.
- [125] Q. Qian, C. Wang, L. Fan, L. Cheng, H. Chen, L. Zhao, *Opt. Mater.* **2021**, *116*, 111103.
- [126] Y. Fan, *Optik* **2019**, *179*, 1084.
- [127] J. T. Lu, et al., *Adv. Funct. Mater.* **2021**, *31*, 9.
- [128] X. Ming, X. Liu, L. Sun, W. J. Padilla, *Opt. Express* **2017**, *25*, 24658.
- [129] Z. Huang, J. Liu, T. Zhang, Y. Jin, J. Wang, S. Fan, Q. Li, *ACS Appl. Mater. Interfaces* **2021**, *13*, 22796.
- [130] N. Zhou, R. Yang, T. Zhai, *Materials Today Nano* **2019**, *8*, 100051.



Alexander Dorodnyy received his B.S. and M.S. from the Moscow Institute of Physics and Technology, Dolgoprudny, Russia, in 2009 and 2011, respectively, and a Ph.D. degree from the Department of Information Technology and Electrical Engineering, ETH Zurich, Zurich, Switzerland, in 2016. Between 2016 and 2018, he worked as a postdoctoral researcher with the Institute of Electromagnetic Fields, ETH Zurich. Since 2018, he has worked as a senior scientist. His research interests include photovoltaic devices, photodetectors, plasmonic devices, tele/data-communication components, photonic meta-surfaces, applications of nanowire structures, numerical methods for photonics, solid-state physics, and machine learning.



Jasmin Smajic received his Ph.D. degree from the Faculty of Electrical Engineering and Computing in Zagreb (Croatia) in 2001. After postdoctoral research at the ETH Zurich from 2002 to 2004 on the topic of full-Maxwell electromagnetic simulations of photonic crystals, he took the position of scientist at the ABB Corporate Research Centre in Baden-Dättwil (Switzerland). Between 2011 and 2020 he was a full professor at the University of Applied Sciences in Rapperswil (Switzerland) and the head of the Computational and Applied Electromagnetics Group. Since 2020, he has worked as a senior scientist and vice-head of the Institute of Electromagnetic Fields at ETH Zurich (Switzerland).



Juerg Leuthold is the head of the Department of Information Science and Electrical Engineering and the head of the Institute of Electromagnetic Fields (IEF) of ETH Zurich, Switzerland. Before his time at ETH, he was affiliated with the Karlsruhe Institute of Technology (KIT) in Germany, where he was the Head of the Institute of Photonics and Quantum Electronics (IPQ) and the Helmholtz Institute of Microtechnology (IMT) from 2004 until 2013. From 1999 to 2004, he was affiliated with Bell Labs, Lucent Technologies, Holmdel, NJ, USA. He received his Ph.D. degree in physics from ETH Zurich in 1998.